Tilted fiber phase gratings

T. Erdogan

The Institute of Optics, University of Rochester, Rochester, New York 14627

J. E. Sipe

Department of Physics, University of Toronto, Toronto, Ontario M5S1A7, Canada

A detailed theoretical treatment is presented of bound-mode to bound-mode Bragg reflection and bound-mode to radiation-mode coupling loss in a tilted optical-fiber phase grating. Numerical predictions of the effects of grating tilt on the spectral characteristics of such a grating are calculated. These predictions are compared with experimentally measured spectra of strong gratings written by ultraviolet irradiation of deuterium-sensitized fiber with grating tilt angles ranging from 0° to 15°. Good agreement is obtained between the theoretical predictions and the experimental results. © 1996 Optical Society of America

1. INTRODUCTION

The fiber phase grating written by ultraviolet (uv) light into the core of an optical fiber has found many useful applications as a wavelength-selective, guided-mode reflector.[1] An important but often less advertised function of the fiber grating is its ability to couple a guided mode to radiation modes of the fiber. This function is sometimes a nuisance, particularly when a complex filter utilizing strictly grating reflection is desired.[2] However, radiation-mode coupling can be used to advantage for fiber taps[3] and broadband filters.[4] Whether radiation-mode coupling is desirable or not, it is useful to understand its origin. A recent paper by Mizrahi and Sipe describes the basic formalism for understanding bound-mode to radiation-mode coupling in a fiber phase grating.[5]

Since the first reported discussions of radiation-mode coupling in fiber gratings, it has been recognized that this coupling can be enhanced and to some extent controlled if a tilt is provided in the fringes of the phase grating.[3,4] This result is obvious from a ray picture of the operation of the grating, in that the tilt functions as a blaze. This picture most clearly demonstrates the ability of a tilted grating to control the directionality of bound-mode to radiation-mode coupling.[3] From a mode picture it is likewise clear why radiation-mode coupling should be enhanced in a tilted grating—with simple symmetry arguments one can show that a LP_{01} bound mode in an untilted grating can couple only to LP radiation modes with azimuthal quantum numbers 0 and 2; in the presence of a tilted grating coupling to all odd radiation modes and all other even radiation modes is allowed as well. In addition simply to enhancing the maximum radiation-mode coupling, variation of grating tilt affects the width of the loss spectrum, the separation of the wavelength region at which maximum radiation-mode coupling occurs from that at which Bragg reflection occurs, and the Bragg reflection spectrum. The last of these is of great importance for filter applications that cannot tolerate any reflection, for which the ability of grating tilt to

diminish Bragg reflection while simultaneously enhancing radiation-mode coupling is advantageous.[4]

In this paper we extend the basic formalism outlined earlier[5] to include tilted fiber phase gratings. Our motivation for developing this theory is to enable the design of filters based on the scattering of a forward-going bound mode into backward-going radiation modes. However, tilted fiber gratings are also important for devices based on bound-mode to bound-mode coupling in both the copropagating and counterpropagating cases and for devices that couple a bound mode into copropagating radiation modes. For the former case the grating tilt enables coupling between bound modes of dissimilar azimuthal symmetry,[6] and the effects of grating tilt in the latter case are analogous to those mentioned above regarding counterpropagating bound-mode to radiation-mode coupling. We will not specifically consider the copropagating coupling (long-period grating) case here, but the formalism that we present can easily be extended to include this case.

In a normal step-index fiber with a finite glass cladding, coupling can occur between the bound core mode and the bound cladding modes of the fiber. These effects are not considered here; we consider only coupling between the bound core mode and the continuum of radiation modes in a fiber with an infinite cladding. Experimentally, the behavior of a bound core mode in an infinite-cladding fiber can be approximately realized by a fiber immersed in or coated with a medium of refractive index equal to or higher than that of the cladding.

We describe in detail in Section 2 the derivation of the coupled-amplitude equations used in this manuscript. The equations are exact, except for one clearly defined approximation that assumes that the refractive index modulation is much smaller than the mode index. In Section 3 we utilize the coupled-amplitude equations to investigate Bragg scattering in the presence of a tilted grating. In addition to a derivation of the theoretical formalism, numerical calculations are described and compared with experimental measurements of the de-

pendence of grating reflectivity on tilt angle for strong gratings written in a step-index fiber. Section 4 describes the theory behind bound-mode to radiation-mode coupling in a tilted grating. Specific attention is paid to the evolution of a bound mode through the grating, with the radiation modes serving as a channel through which the bound mode loses energy. The treatment closely parallels that of spontaneous emission of an atom from its excited state, first described by Wigner and Weiskopff. In Section 5 the extinction coefficients that describe the loss of bound-mode energy to radiation modes are described in detail. Section 6 contains numerical predictions of the dependence of radiation-mode loss spectra on grating tilt angle based on the theory described in the previous sections. These predictions are again compared with experimental measurements of transmission spectra from gratings written with tilt angles ranging from 0° to 15°. Finally, conclusions are drawn in Section 7.

2.　MODE AMPLITUDE EQUATIONS

In this section we derive the equations for the spatially varying amplitudes of the bound and radiation modes of an ideal fiber in the presence of a variation in the local index of refraction that is due to a grating structure. The technique is an extension of a method employed earlier by one of us[7] to consider coupling between bound modes in planar waveguide structures, and in fact the results of this section hold quite generally for any guiding structure. Treatments of coupling between modes of a guiding structure abound (see, e.g., Ref. 8), but the Green-function approach employed here has the advantage that the effect of source polarizations on the mode amplitudes [see Eqs. (2.12) below] is described exactly.[7] For the problem of interest here, where the source polarization is due to a grating, the resulting coupled-amplitude equations [Eqs. (2.21) and (2.22) below] are similarly essentially exact and do not appear to have been written down before. With such exact equations as a starting point it is easier to keep track of the subsequent approximations (see Sections 3–5) necessary and desirable to construct a concise treatment of the phenomena of interest.

We consider fields oscillating at frequency ω and introduce a field amplitude $\mathbf{E}$ for the electric field $\boldsymbol{\varepsilon}$:

$$\boldsymbol{\varepsilon}(\mathbf{R}, t) = \mathbf{E}(\mathbf{R})\exp(-i\omega t) + \text{c.c.} \qquad (2.1)$$

Choosing the fiber axis to lie along the z axis, we find it convenient to denote separately the electric-field component along this axis, $E^z(x, y, z)$, and the components transverse to it,

$$\mathbf{E}^t(x, y, z) = \hat{x}E^x(x, y, z) + \hat{y}E^y(x, y, z). \qquad (2.2)$$

Adopting the same notation for the magnetic field, we schematically denote the electromagnetic field amplitude by $F(x, y, z)$, identifying the different components in a column vector as follows:

$$F(x, y, z) = \begin{pmatrix} E^z(x, y, z) \\ H^z(x, y, z) \\ \mathbf{E}^t(x, y, z) \\ \mathbf{H}^t(x, y, z) \end{pmatrix}. \qquad (2.3)$$

Consider first an ideal fiber, where the index of refraction depends only on x and y and often in fact only on $\sqrt{x^2 + y^2}$. The types of modes here[9] can be labeled by (α, p). The variable α can be discrete (indicated by m) or continuous (indicated by ρ) and characterizes the propagation of the mode in the z direction. The propagation constants along the fiber axis we take to be $\pm\beta_m$ (discrete modes) or $\pm\beta(\rho)$ (continuous modes); p specifies any other degeneracy indices. Thus, to specify a mode and a direction (propagation in the $+z$ or $-z$ direction), we need a sign ($\pm$) as well as (α, p). The electromagnetic field of a mode propagating in the $+z$ direction is of the form

$$\begin{pmatrix} E^{+z}_{\alpha p}(x, y) \\ H^{+z}_{\alpha p}(x, y) \\ \mathbf{E}^{+t}_{\alpha p}(x, y) \\ \mathbf{H}^{+t}_{\alpha p}(x, y) \end{pmatrix}\exp(i\beta_\alpha z) \equiv \begin{pmatrix} e^z_{\alpha p}(x, y) \\ h^z_{\alpha p}(x, y) \\ \mathbf{e}^t_{\alpha p}(x, y) \\ \mathbf{h}^t_{\alpha p}(x, y) \end{pmatrix}\exp(i\beta_\alpha z)$$

$$\equiv f^+_{\alpha p}(x, y)\exp(i\beta_\alpha z), \qquad (2.4)$$

and that of the corresponding mode propagating in the $-z$ direction is

$$\begin{pmatrix} E^{-z}_{\alpha p}(x, y) \\ H^{-z}_{\alpha p}(x, y) \\ \mathbf{E}^{-t}_{\alpha p}(x, y) \\ \mathbf{H}^{-t}_{\alpha p}(x, y) \end{pmatrix}\exp(-i\beta_\alpha z) \equiv \begin{pmatrix} -e^z_{\alpha p}(x, y) \\ h^z_{\alpha p}(x, y) \\ \mathbf{e}^t_{\alpha p}(x, y) \\ -\mathbf{h}^t_{\alpha p}(x, y) \end{pmatrix}\exp(-i\beta_\alpha z)$$

$$\equiv f^-_{\alpha p}(x, y)\exp(-i\beta_\alpha z). \qquad (2.5)$$

The modes are chosen to be power orthogonal; for discrete modes we put

$$\int (\mathbf{e}^t_{mp} \times \mathbf{h}^{t*}_{m'p'}) \cdot \hat{z}\, \mathrm{d}s = \tfrac{1}{2}P_{mp}\delta_{mm'}\delta_{pp'}, \qquad (2.6)$$

for continuous modes we put

$$\int (\mathbf{e}^t_{\rho p} \times \mathbf{h}^{t*}_{\rho'p'}) \cdot \hat{z}\, \mathrm{d}s = \tfrac{1}{2}P_p(\rho)\delta(\rho - \rho')\delta_{pp'}, \qquad (2.7)$$

and we have

$$\int (\mathbf{e}^t_{mp} \times \mathbf{h}^{t*}_{\rho'p'}) \cdot \hat{z}\, \mathrm{d}s = 0, \qquad \text{etc.} \qquad (2.8)$$

The ρ that appears in Eq. (2.7) and as a label of the continuous modes is taken as usual[9] to be

$$\rho = \sqrt{n_{\mathrm{cl}}^2 k^2 - \beta^2}, \qquad (2.9)$$

where $k \equiv \omega/c$ and n_{cl} is the index of refraction of the (outermost) cladding. Here the P_{mp} and $P_p(\rho)$ are normalization constants; integrals over $\mathrm{d}s \equiv \mathrm{d}x\mathrm{d}y$ [as in Eqs. (2.6)–(2.8) and below] range over the x–y plane; δ indicates a Kronecker delta or Dirac delta function, as the argument(s) are discrete or continuous, respectively. Our notation largely follows that of Ref. 9, but with the following exceptions: we use the $-i\omega t$ convention rather than the $+i\omega t$ convention [Eq. (2.1)]; we explicitly indicate the $\pm$ propagation direction of the modes (so our β_α's are always positive); and we use no factor of $1/2$ in Eq. (2.1), inserting it instead in Eqs. (2.6) and (2.7). We have assumed that the index of refraction is real but otherwise an arbitrary function of x and y, $n_0(x, y)$. As

have most workers, we neglect any effects associated with evanescent radiation modes of the fiber.[9]

Now consider the ideal fiber in the presence of a perturbation that is due to a source polarization, a dipole moment per unit volume $\mathbf{P}(\mathbf{R})$ not described implicitly by $n_0(x, y)$. The field that is due to this polarization can essentially be found exactly, a calculation that is outlined in Appendix A. It consists of two parts; one is an electric field $\mathbf{E}^d(\mathbf{R})$ given simply by

$$\mathbf{E}^d(x, y, z) = \frac{-\hat{z}P^z(x, y, z)}{\epsilon_0 n_0^2(x, y)}, \qquad (2.10)$$

and the rest can be written as a superposition of modes of the ideal fiber, but with spatially varying amplitudes. The latter we call the modes part of the field, and it is given by

$$F(x, y, z) = \sum_{\alpha p} \tilde{a}_{\alpha p}^+(z) f_{\alpha p}^+(x, y) \exp(i\beta_\alpha z)$$
$$+ \sum_{\alpha p} \tilde{a}_{\alpha p}^-(z) f_{\alpha p}^-(x, y) \exp(-i\beta_\alpha z), \qquad (2.11)$$

where the mode coefficients satisfy

$$\frac{d\tilde{a}_{\alpha p}^+(z)}{dz} = \frac{i\omega}{P_{\alpha p}} \exp(-i\beta_\alpha z) \int \mathbf{P}(x, y, z) \cdot \mathbf{E}_{\alpha p}^{+*}(x, y) ds,$$
$$\frac{d\tilde{a}_{\alpha p}^-(z)}{dz} = \frac{-i\omega}{P_{\alpha p}} \exp(i\beta_\alpha z) \int \mathbf{P}(x, y, z) \cdot \mathbf{E}_{\alpha p}^{-*}(x, y) ds,$$
$$(2.12)$$

and the integrals range over the $x-y$ plane.

Up to this point the expressions that we have derived for the two components [Eqs. (2.10 and 2.11)] of the electromagnetic field generated by the source polarization are completely general; the source polarization could be due to any of a number of physical effects, including optical nonlinearities or corrugations in the interfaces. We have, as mentioned, omitted the evanescent radiation modes from the analysis, but even with that omission the expressions for the mode components that we have included are exact. Now we specialize to a source polarization that is due to a grating structure in the fiber; that is, we take

$$\mathbf{P}(x, y, z) = \epsilon_0 \Delta\chi \mathbf{E}(x, y, z), \qquad (2.13)$$

where $\Delta\chi$ is a variation in the susceptibility, the position dependence of which we specify presently, and the electric field indicated is the full electric field. We put $\Delta\chi \equiv 2\bar{n}\Delta n(x, y, z)$, where $\Delta n(x, y, z)$ is a spatially varying effective refractive index and $\bar{n}$ is a reference refractive index. For small variations in the dielectric constant these may of course be taken to be the actual spatially varying refractive index and, say, the cladding index of refraction, respectively. Then we have

$$\mathbf{P}(x, y, z) = 2\epsilon_0 \bar{n} \Delta n(x, y, z) \mathbf{E}(x, y, z)$$
$$= 2\epsilon_0 \bar{n} \Delta n(x, y, z)[\mathbf{E}_{\text{modes}}(x, y, z) + \mathbf{E}^d(x, y, z)], \qquad (2.14)$$

where in the second of Eqs. (2.14) we have written the electric field as the sum of the two parts discussed above, the modes subscript indicating the portion of the field

from Eq. (2.11). Now, splitting the polarization into its component along the fiber axis and those components perpendicular to the axis and using Eq. (2.10), we may write

$$\mathbf{P}^t(x, y, z) = 2\epsilon_0 \bar{n} \Delta n(x, y, z) \mathbf{E}_{\text{modes}}^t(x, y, z),$$
$$P^z(x, y, z) = \frac{2\epsilon_0 \bar{n} \Delta n(x, y, z) E_{\text{modes}}^z(x, y, z)}{1 + \frac{2\bar{n}\Delta n(x, y, z)}{n_0^2(x, y)}}. \qquad (2.15)$$

For simplicity we now assume that the variation in the (effective) refractive index is small compared with the local index in the ideal fiber, i.e., $\Delta n(x, y, z) \ll n_0(x, y, z)$. Even in the strongest fiber gratings written to date, this is a good approximation. Then, neglecting the $\Delta n(x, y, z)$ term in the denominator of the second of Eqs. (2.15), we find

$$\mathbf{P}(x, y, z) \simeq 2\epsilon_0 \bar{n} \Delta n(x, y, z) \mathbf{E}_{\text{modes}}(x, y, z), \qquad (2.16)$$

which is the form that we use for the source polarization, taking the effective variation in the refractive index to be in fact the actual variation. We now specify the general form of that variation.

The gratings of interest to us here are written by the interference of two coherent ultraviolet beams. The spatially varying uv intensity leads, by a process not yet completely understood, to a rise in the refractive index that, at least to good approximation, is highest where the local intensity is highest. In the usual instance of a pure silica cladding the index change occurs only in the fiber core. Thus we introduce a function $\zeta(x, y)$, which is equal to unity in the fiber core and vanishes elsewhere, and write

$$\frac{\Delta n(x, y, z)}{\bar{n}} = \zeta(x, y) \eta(z'), \qquad (2.17)$$

where $\eta(z')$ is a function that specifies the index variation in the fiber core. We consider a geometry in which the wave vector associated with the interference of the two beams makes an angle θ from the fiber axis and lies in a plane that we take to be the $x-z$ plane (see Fig. 1). Thus the natural variable for the function $\eta(z')$ is $z' = z\cos\theta + x\sin\theta$. Now, on the length scale set by the interference wave vector, the intensity of the uv light will be a slowly varying function of position that is due, for example, to the shape of the writing beams. We also wish to allow for possible chirping of the grating. Thus, for the function $\eta(z')$, we take

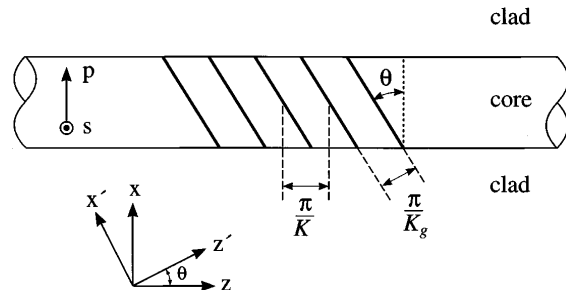$$\eta(z') = \bar{\sigma}(z') + 2\bar{\kappa}(z')\cos[2K_g z' + \bar{\phi}(z')]. \qquad (2.18)$$

Fig. 1. Diagram of the core of a step-index optical fiber showing a tilted fiber phase grating and definitions used in the analysis.

Here $2K_g$ is the nominal wave number of the grating, and the function $\bar{\phi}(z')$, assumed to be slowly varying on a length scale set by the nominal wave number, can describe a position-dependent chirp. The other slowly varying functions, $2\bar{\kappa}(z')$ and $\bar{\sigma}(z')$, describe the grating amplitude and the concomitant slowly varying perturbation in the background index of refraction that accompanies the grating writing[5]; the unsightly factor of 2 in the grating amplitude is introduced to ensure a simple form for later equations [see, e.g., Eqs. (2.21) and (2.22)]. Higher Fourier components (i.e., multiples of $2K_g$) are neglected. They can have two physically distinct effects: First, they will lead to scattering associated with multiples of $2K_g$; this can be described simply by the addition of more terms to Eq. (2.18) but will not be important at the wavelengths of interest in this paper. Second, they will modify the scattering associated with the fundamental wave number $2K_g$ (Ref. 10); these effects can be included in the coupled-mode equations that we derive in Section 3, but at grating strengths of current interest they will be small [see the discussion after Eqs. (3.1)]. Thus it is sufficient to restrict ourselves to Eq. (2.18).

Since $\eta(z')$ is required only at points in the fiber core [see Eq. (2.17)], it is permissible in the slowly varying functions to put $z' = z\cos\theta + x\sin\theta \approx z\cos\theta$. Further, to simplify the notation, we define corresponding unbarred functions,

$$\sigma(z) \equiv \bar{\sigma}(z\cos\theta), \qquad \phi(z) \equiv \bar{\phi}(z\cos\theta),$$

$$\kappa(z) \equiv \bar{\kappa}(z\cos\theta), \qquad \kappa_c(z) \equiv \kappa(z)\exp[i\phi(z)], \quad (2.19)$$

in terms of which we write the source polarization (2.16),

$$\begin{aligned}
\mathbf{P}(x, y, z) = {}& 2\epsilon_0 \bar{n}^2 \zeta(x, y)\{\sigma(z) + \kappa_c(z) \\
& \times \exp[2iK(z + x\tan\theta)] \\
& + \kappa_c^*(z)\exp[-2iK(z + x\tan\theta)]\} \\
& \times \mathbf{E}_{\text{modes}}(x, y, z). \quad (2.20)
\end{aligned}$$

Here $2K \equiv 2K_g\cos\theta$ is the grating wave-vector component along the fiber axis. Now, inserting Eq. (2.20) in Eqs. (2.12) and expanding the field that is due to the modes, we find a set of coupled-amplitude equations. For modes going to the right ($+z$) we find that

$$\begin{aligned}
\bar{\beta}^{-1}\frac{\mathrm{d}a_\alpha^+}{\mathrm{d}z} \\
= i\sigma(z)&\Bigg\{\sum_{\alpha'} g_{\alpha\alpha'}^{++}a_{\alpha'}^+(z)\exp[i(\beta_{\alpha'} - \beta_\alpha)z] \\
& + \sum_{\alpha'} g_{\alpha\alpha'}^{+-}a_{\alpha'}^-(z)\exp[i(-\beta_{\alpha'} - \beta_\alpha)z]\Bigg\} \\
+ i\kappa_c(z)\exp(2iKz)&\Bigg\{\sum_{\alpha'} \mu_{\alpha\alpha'}^{++}a_{\alpha'}^+(z)\exp[i(\beta_{\alpha'} - \beta_\alpha)z] \\
& + \sum_{\alpha'} \mu_{\alpha\alpha'}^{+-}a_{\alpha'}^-(z)\exp[i(-\beta_{\alpha'} - \beta_\alpha)z]\Bigg\} \\
+ i\kappa_c^*(z)\exp(-2iKz)&\Bigg\{\sum_{\alpha'} \nu_{\alpha\alpha'}^{++}a_{\alpha'}^+(z)\exp[i(\beta_{\alpha'} - \beta_\alpha)z] \\
& + \sum_{\alpha'} \nu_{\alpha\alpha'}^{+-}a_{\alpha'}^-(z)\exp[i(-\beta_{\alpha'} - \beta_\alpha)z]\Bigg\}, \quad (2.21)
\end{aligned}$$

and for modes going to the left we obtain

$$\begin{aligned}
\bar{\beta}^{-1}\frac{\mathrm{d}a_\alpha^-}{\mathrm{d}z} \\
= -i\sigma(z)&\Bigg\{\sum_{\alpha'} g_{\alpha\alpha'}^{-+}a_{\alpha'}^+(z)\exp[i(\beta_{\alpha'} + \beta_\alpha)z] \\
& + \sum_{\alpha'} g_{\alpha\alpha'}^{--}a_{\alpha'}^-(z)\exp[i(-\beta_{\alpha'} + \beta_\alpha)z]\Bigg\} \\
- i\kappa_c(z)\exp(2iKz)&\Bigg\{\sum_{\alpha'} \mu_{\alpha\alpha'}^{-+}a_{\alpha'}^+(z)\exp[i(\beta_{\alpha'} + \beta_\alpha)z] \\
& + \sum_{\alpha'} \mu_{\alpha\alpha'}^{--}a_{\alpha'}^-(z)\exp[i(-\beta_{\alpha'} + \beta_\alpha)z]\Bigg\} \\
- i\kappa_c^*(z)\exp(-2iKz)&\Bigg\{\sum_{\alpha'} \nu_{\alpha\alpha'}^{-+}a_{\alpha'}^+(z)\exp[i(\beta_{\alpha'} + \beta_\alpha)z] \\
& + \sum_{\alpha'} \nu_{\alpha\alpha'}^{--}a_{\alpha'}^-(z)\exp[i(-\beta_{\alpha'} + \beta_\alpha)z]\Bigg\}. \quad (2.22)
\end{aligned}$$

Here, for simplicity, we adopt a shorthand for indicating the set of indices characterizing the mode type, using α and α', for example, to denote (α, p) and (α', p'). We have also introduced mode amplitudes defined without the power normalization factor,

$$a_\alpha^\pm \equiv \sqrt{\tfrac{1}{2}P_\alpha}\, \tilde{a}_\alpha^\pm, \quad (2.23)$$

and a reference wave number

$$\bar{\beta} \equiv \frac{\omega}{c}\,\bar{n}. \quad (2.24)$$

The coupling constants appearing in Eqs. (2.21) and (2.22) that mediate the interaction between the modes that is due to the slowly varying perturbation in the background index of refraction are

$$g_{\alpha\alpha'}^{ij} \equiv \frac{2\bar{n}c\epsilon_0}{\sqrt{P_\alpha P_{\alpha'}}}\int \mathbf{E}_\alpha^{i*}(x, y)\cdot\zeta(x, y)\mathbf{E}_{\alpha'}^j(x, y)\mathrm{d}s, \quad (2.25)$$

where i and j can be $+$ or $-$. Likewise, the coupling constants that mediate the interaction that is due to the $+2K$ component of the grating [see Eq. (2.20)] are given by

$$\begin{aligned}
\mu_{\alpha\alpha'}^{ij} \equiv {}& \frac{2\bar{n}c\epsilon_0}{\sqrt{P_\alpha P_{\alpha'}}}\int \mathbf{E}_\alpha^{i*}(x, y)\exp[2iKx(\tan\theta)] \\
& \cdot \zeta(x, y)\mathbf{E}_{\alpha'}^j(x, y)\mathrm{d}s, \quad (2.26)
\end{aligned}$$

and those that mediate the interaction that is due to the $-2K$ component of the grating are given by

$$\begin{aligned}
\nu_{\alpha\alpha'}^{ij} \equiv {}& \frac{2\bar{n}c\epsilon_0}{\sqrt{P_\alpha P_{\alpha'}}}\int \mathbf{E}_\alpha^{i*}(x, y)\exp[-2iKx(\tan\theta)] \\
& \cdot \zeta(x, y)\mathbf{E}_{\alpha'}^j(x, y)\mathrm{d}s. \quad (2.27)
\end{aligned}$$

For an untilted grating ($\theta = 0$; see Fig. 1) we have $g_{\alpha\alpha'}^{ij} = \mu_{\alpha\alpha'}^{ij} = \nu_{\alpha\alpha'}^{ij}$, but more generally the constants can be quite different.

The coupled-amplitude equations (2.21) and (2.22) are the main result of this section. Except for the mi-

nor approximation involved in replacing Eq. (2.18) with Eqs. (2.19) and the neglect of the evanescent radiation modes, they are exact. However, insofar as they involve a sum over an infinite number of modes, they are intractable. In the following sections we simplify them, using the physically appropriate approximations, to treat the various phenomena of interest.

3.   BRAGG SCATTERING

Perhaps the simplest scattering geometry involves a grating wave number $2K$ adjusted to scatter a discrete mode propagating to the right $(+z)$ to the corresponding discrete mode propagating to the left $(-z)$. We consider this, the geometry of Bragg scattering, in this section. For simplicity we will adopt the LP approximation for the fiber modes, appropriate for the weakly guiding fibers of interest in optical communications, and further approximate the refractive index profile $n_0(x, y)$ as varying stepwise at a radius a from a core index n_{core} to a cladding index n_{cl}; we take the cladding to be infinite in extent. The electromagnetic field profiles associated with these modes [Eqs. (2.4) and (2.5)] are given in a number of texts.[9]

Of primary interest is the lowest (and often only) discrete mode LP_{01}. Here we use the discrete index $\alpha = m = (01)$, reserving the index p to label the two polarizations. In the simplest case of untilted gratings $(\theta = 0)$, which we consider first, symmetry prohibits scattering from a mode of one polarization to that of another. Then the coupling constants that will be of interest are

$$g_{01;01}^{--} = g_{01;01}^{++} = \frac{2\bar{n}c\epsilon_0}{P_{01}} \int \mathbf{E}_{01}^{+*}(x, y) \cdot \zeta(x, y)\mathbf{E}_{01}^{+}(x, y)\mathrm{d}s$$
$$\equiv g_f,$$

$$\mu_{01;01}^{+-} = (\nu_{01;01}^{-+})^* = \frac{2\bar{n}c\epsilon_0}{P_{01}} \int \mathbf{E}_{01}^{+*}(x, y) \cdot \zeta(x, y)\mathbf{E}_{01}^{-}(x, y)\mathrm{d}s$$
$$\equiv g_b, \qquad (3.1)$$

where evaluation confirms that both g_f and g_b are real. If $\beta_{01} \simeq K$, then the only phase-matched terms in Eqs. (2.21) and (2.22) are those involving the coefficients in Eqs. (3.1). The usual heuristic approach is simply to neglect the non-phase-matched terms. The validity of this approximation can be investigated with a more rigorous calculation,[10] which also leads to corrections to that simple approach; they are generally negligible for grating strengths of interest, as are the corrections that are due to higher-order Fourier components [see the comments after Eq. (2.18)]. But this is a point to which we return in Section 7. In the usual approximation of keeping only the phase-matched terms, Eqs. (2.21) and (2.22) reduce to

$$\bar{\beta}^{-1} \frac{\mathrm{d}a_{01}^+}{\mathrm{d}z} = i g_f \sigma(z)a_{01}^+(z) + i g_b \kappa(z)\exp[i\phi(z)]$$
$$\times \exp[2i(K - \beta_{01})z]a_{01}^-(z),$$

$$\bar{\beta}^{-1} \frac{\mathrm{d}a_{01}^-}{\mathrm{d}z} = - i g_f \sigma(z)a_{01}^-(z) - i g_b \kappa(z)\exp[-i\phi(z)]$$
$$\times \exp[-2i(K - \beta_{01})z]a_{01}^+(z). \qquad (3.2)$$

The first terms on the right-hand sides of Eqs. (3.2) de-

scribe the forward scattering of each mode, which is due to the background change in the overall index of refraction that accompanies the grating formation [see Eq. (2.18)]; the second terms describe the backward scattering, the Bragg scattering that is due to the grating. If we introduce new variables,

$$u(z) \equiv a_{01}^+(z)\exp[\tfrac{1}{2}i\phi(z)]\exp[-i(K - \beta_{01})z],$$
$$v(z) \equiv a_{01}^-(z)\exp[\tfrac{1}{2}i\phi(z)]\exp[i(K - \beta_{01})z], \qquad (3.3)$$

Eqs. (3.2) take the form

$$\bar{\beta}^{-1} \frac{\mathrm{d}u}{\mathrm{d}z} = i\left[g_f \sigma(z) + \delta - \frac{1}{2} \bar{\beta}^{-1} \frac{\mathrm{d}\phi}{\mathrm{d}z} \right]u(z)$$
$$+ i g_b \kappa(z)v(z),$$

$$\bar{\beta}^{-1} \frac{\mathrm{d}v}{\mathrm{d}z} = - i\left[g_f \sigma(z) + \delta - \frac{1}{2} \bar{\beta}^{-1} \frac{\mathrm{d}\phi}{\mathrm{d}z} \right]v(z)$$
$$- i g_b \kappa(z)u(z), \qquad (3.4)$$

where

$$\delta \equiv \frac{\beta_{01} - K}{\bar{\beta}} \qquad (3.5)$$

specifies the detuning from the Bragg resonance condition. In the weakly guiding approximation we have $\beta_{01}a \simeq n_{\mathrm{cl}}ka[1 + b_{01}(V)\Delta]$, where $b_{01}(V)$ is Gloge's[11] normalized propagation constant function, $V \simeq \sqrt{2\Delta}\,n_{\mathrm{cl}}ka$ is the V number of the mode, and $\Delta \equiv (n_{\mathrm{core}} - n_{\mathrm{cl}})/n_{\mathrm{cl}}$. Since $\Delta \ll 1$ and we may take $\bar{\beta} \simeq K$ reasonably near the Bragg resonance, to lowest order in the effective detuning from the Bragg resonance we have

$$\delta \simeq \frac{\omega - \omega_{\mathrm{Bragg}}}{\omega_{\mathrm{Bragg}}}, \qquad (3.6)$$

where ω_{Bragg} is the nominal frequency of the Bragg scattering resonance associated with the scattering wave number $2K$. Thus δ can essentially be identified as the frequency detuning from that resonance.

Equations (3.4) are then seen to take the form of the usual coupled-mode equations that one would write down for scattering from a grating in a purely one-dimensional problem,[12] except for the presence of the factors g_f and g_b. These factors clearly describe how effective the grating perturbation is in leading to forward and backward scattering, respectively. In the weakly guiding limit the expressions (3.1) for g_f and g_b can easily be evaluated with use of the well-known LP_{01} mode profiles. We find that $g_f = g + \tilde{g}$ and $g_b = g - \tilde{g}$, where

$$g = b_{01}\left[\frac{J_0^2(\kappa_{01}a)}{J_1^2(\kappa_{01}a)} + 1 \right],$$
$$\tilde{g} = \frac{\Delta b_{01}(1 - b_{01})}{1 + 2\Delta b_{01}}\left[1 - \frac{J_0(\kappa_{01}a)J_2(\kappa_{01}a)}{J_1^2(\kappa_{01}a)} \right]. \qquad (3.7)$$

Here κ_{01} is the wave number characterizing the variation of the field through the fiber core in the LP_{01} mode, $\kappa_{01}a = V\sqrt{1 - b_{01}}$. The coefficients of Eqs. (3.7) are plotted in
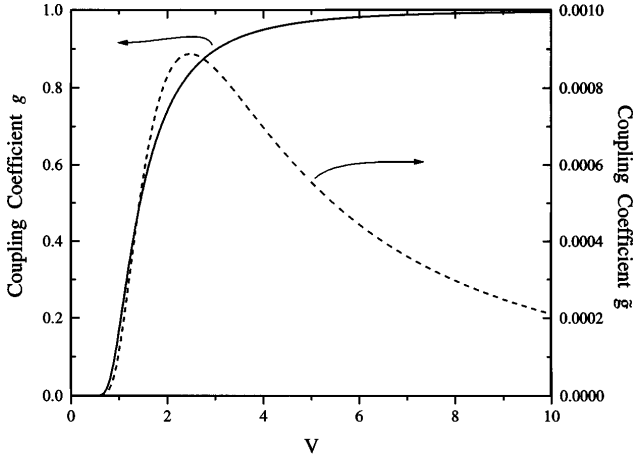
Fig. 2. Plots of the two terms g and $\tilde{g}$ that contribute to the forward and backward coupling coefficients g_f and g_b, respectively, defined in Eqs. (3.1). Note that $\tilde{g} \ll g$.

Fig. 2 as a function of V for the choice $\Delta = 0.0055$. With reference to Eqs. (3.1), it is clear that g_f and g_b differ only because of the z component of the electric field in the LP_{01} mode. Since this component is typically much smaller than the transverse components, we expect and find that, to good approximation, $g_f \approx g_b \approx g$; that is, to good approximation, the grating is equally efficient in forward and backward scattering. Further, g is equal to the fraction of the mode power carried in the core[9]; since the grating is by assumption confined to the core of the fiber, the resulting conclusion that the grating is effective in scattering to the extent that the fiber mode is confined to the core is not unexpected.

We now turn to the more complicated problem of tilted gratings. Referring back to Eqs. (2.25)–(2.27), we see that the first of Eqs. (3.1) is unmodified by a nonzero θ, but the second is not. The new expression for g_b, which must be used in the coupled-mode equations (3.4), is

$$
\begin{aligned}
\mu_{01;01}^{+-} &= (\nu_{01;01}^{-+})^* \\
&= \frac{2\bar{n}c\epsilon_0}{P_{01}} \int \mathbf{E}_{01}^{+*}(x, y)\exp[2iKx(\tan\theta)] \\
&\quad \cdot \zeta(x, y)\mathbf{E}_{01}^{-}(x, y)\mathrm{d}s \\
&\equiv g_b .
\end{aligned}
\tag{3.8}
$$

For arbitrary θ, even with the LP approximation, Eq. (3.8) can be evaluated only numerically. We find two different expressions, depending on whether the mode is s-polarized or p-polarized with respect to the grating (Fig. 1). For the first geometry we find that

$$
\begin{aligned}
&\frac{(\kappa_{01}a)^2 J_1{}^2(\kappa_{01}a)g_b(s\text{-polarized})}{2b_{01}} \\
&= \int_0^{\kappa_{01}a} J_0{}^2(u)J_0(\Omega u)u\,\mathrm{d}u - \frac{2\Delta(1 - b_{01})}{1 + 2\Delta b_{01}} \\
&\quad \times \int_0^{\kappa_{01}a} \frac{J_1(\Omega u)}{\Omega u}J_1{}^2(u)u\,\mathrm{d}u
\end{aligned}
\tag{3.9}
$$

and for the second we find that

$$
\begin{aligned}
&\frac{(\kappa_{01}a)^2 J_1{}^2(\kappa_{01}a)g_b(p\text{-polarized})}{2b_{01}} \\
&= \int_0^{\kappa_{01}a} J_0{}^2(u)J_0(\Omega u)u\,\mathrm{d}u - \frac{2\Delta(1 - b_{01})}{1 + 2\Delta b_{01}} \\
&\quad \times \int_0^{\kappa_{01}a} J_1{}^2(u)J_0(\Omega u)u\,\mathrm{d}u + \frac{2\Delta(1 - b_{01})}{1 + 2\Delta b_{01}} \\
&\quad \times \int_0^{\kappa_{01}a} J_1{}^2(u)\frac{J_1(\Omega u)}{\Omega u}u\,\mathrm{d}u .
\end{aligned}
\tag{3.10}
$$

In both these expressions $\Omega \equiv (2K\tan\theta)/\kappa_{01}$. In practice the two expressions (3.9) and (3.10) differ little over the small range of θ for which their values are significant. The second term in Eq. (3.9) and the second and third terms in Eq. (3.10) result from the z component of the field in the LP_{01} mode and lead to contributions that are small; to good approximation, both $g_b(s$-polarized) and $g_b(p$-polarized) are given by the first terms in their corresponding expressions. In Fig. 3 we show the dropoff of g_b with increasing tilt angle for the following choice of fiber parameters: core radius $a = 2.625$ μm, cladding index $n_{cl} = 1.44$, and $\Delta = 0.0055$. These parameters describe the Corning Flexcore fiber that we used in the experiments. Unless otherwise noted, all calculations described below utilize this set of parameters.

We now describe numerical calculations and experimental results that illustrate the range of phenomena that the coupled-mode equations (3.4) can describe. Note that regardless of the chirp, or the coupling constants, or the variation in the grating amplitude and background index profile, Eqs. (3.4) satisfy energy conservation in the form

$$
\frac{\mathrm{d}}{\mathrm{d}z}[|u(z)|^2 - |v(z)|^2] = 0 .
\tag{3.11}
$$

That is, the flux of energy through the fiber is uniform. Thus the reflection and the transmission of the grating structure, which must in general be calculated by numerical solution of Eqs. (3.4), will always sum to unity.

The coupled mode equations (3.4) must be solved numerically through the fiber profile, and to simplify the
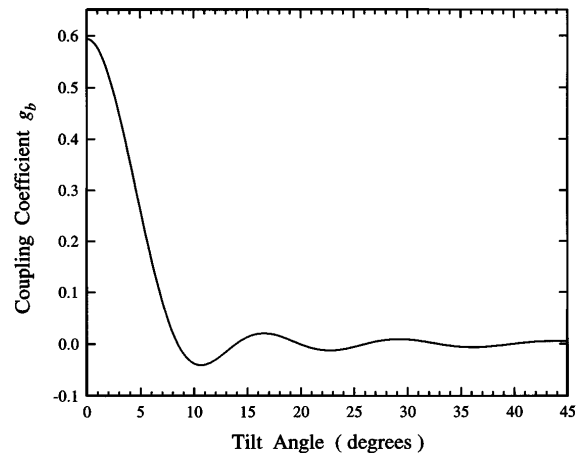

Fig. 3. Plot of backward coupling coefficient versus grating tilt angle for the fiber parameters described in the text.
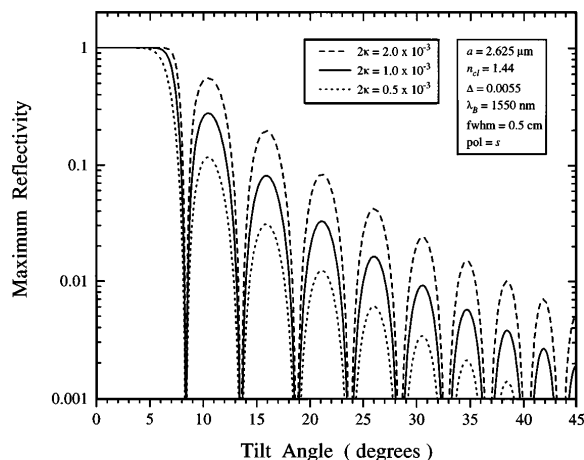
Fig. 4. Calculated maximum grating reflectivity versus grating tilt angle for gratings with three different index modulations and assuming s-polarized incident light and the fiber parameters listed.

calculation, we evaluate g_f and g_b at the design frequency and approximate δ by relation (3.6). Over the range of frequencies of interest these approximations are certainly adequate. Figure 4 shows a calculation of the peak reflectivity versus grating tilt angle, θ, for several grating amplitudes: $2\kappa = 2.0 \times 10^{-3}$ (dashed), $2\kappa = 1.0 \times 10^{-3}$ (solid), and $2\kappa = 0.5 \times 10^{-3}$ (dotted). Here the grating is taken to have 100% modulation [$\sigma = 2\kappa$ in Eq. (2.18)] with a Gaussian profile of full width at half-maximum (FWHM) of 5 mm, and the design wavelength is 1550 nm. Note that the locations of the reflectivity nulls are independent of grating amplitude. In Fig. 5 calculated reflectivity spectra are plotted versus grating tilt angle. Again, plots are made for grating amplitudes of (a) $2\kappa = 2.0 \times 10^{-3}$, (b) $2\kappa = 1.0 \times 10^{-3}$, and (c) $2\kappa = 0.5 \times 10^{-3}$. The curves in Figs. 4 and 5 were calculated for s polarization, but curves for p polarization are indistinguishable on these plots.

The modulation on the short-wavelength side of the reflectivity spectra occurs even at zero tilt angle and for gratings with perfect (100%) index modulation and results from the effective Fabry–Perot cavity formed by the wings of these Gaussian-profile gratings—it is possible for short wavelengths to lie within the band gap associated with the wings but not within the band gap associated with the center of the grating, on account of its higher average refractive index.[5] For an untilted grating a reduction in modulation [$2\kappa < \sigma$ in Eq. (2.18)] exacerbates this effect. In an analogous fashion, because the presence of a tilt effectively reduces the scattering associated with the grating amplitude, 2κ, but not that associated with the background index, σ [see Eqs. (2.21), (2.22), and (2.25)–(2.27)], the reflectivity spectra of gratings at high tilt angles are dominated by this Fabry–Perot modulation.

To investigate the dependence of reflectivity on tilt angle experimentally, we wrote a set of nominally identical gratings at various tilt angles. Corning Flexcore fiber was chosen for these experiments because of its nearly step-index profile. The fiber had a core radius of approximately $a = 2.625\ \mu$m and $\Delta = 0.0055$. It was loaded with approximately 3.8 mol. % of deuterium for enhancement
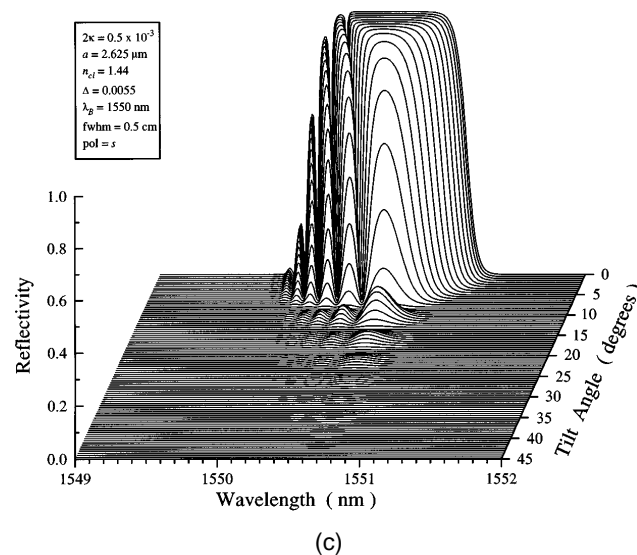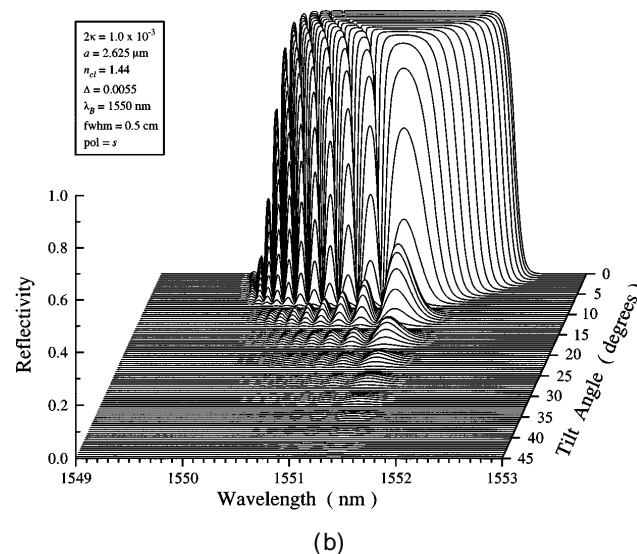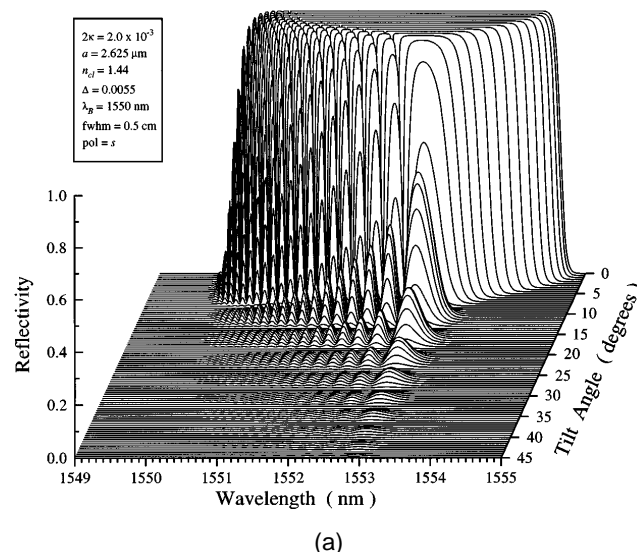

(a)

(b)

(c)

Fig. 5. Calculated grating reflectivity spectra versus tilt angle for gratings with three different index modulations and assuming s-polarized incident light and the fiber parameters listed.
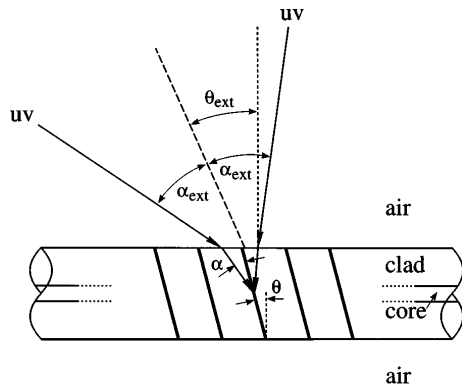
Fig. 6. Diagram showing rays that represent the two uv beams incident on the fiber during grating writing and their associated angles inside and outside the fiber.
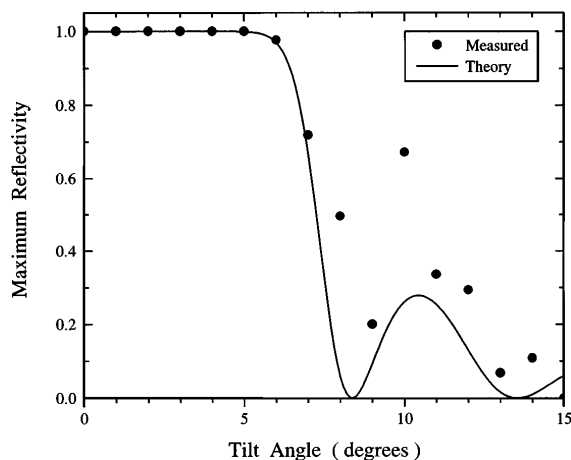

Fig. 7. Experimentally measured maximum grating reflectivity (circles) for gratings written with tilt angles of $0°-15°$. The solid line shows the calculated result.

of its photosensitivity.[13] We wrote gratings by interfering two beams from a 242-nm excimer-laser-pumped, frequency-doubled dye laser producing 15-ns pulses at a 30-Hz repetition rate. Exposures were done with 20 mW of average power, with the nearly Gaussian beam focused to a spot size of approximately 5 mm $\times$ 50 μm on the fiber. Exposure times varied from 1 to 2 min; the transmission spectrum was monitored in real time to achieve roughly the same uv-induced index change for all gratings. However, due to variations in interferometer alignment from grating to grating, there is a noticeable variation in both grating modulation and uv-induced index change among the gratings.

The grating tilt was achieved by rotation of the fiber about the axis normal to the plane defined by the two intersecting uv beams (see Fig. 6). Using Snell's law, one can write a grating with a design wavelength of λ_B^0 and a grating tilt angle of θ by using a uv-beam intersection angle in air of $2\alpha_{\text{ext}}$ and an external tilt angle θ_{ext} given by

$$2\alpha_{\text{ext}} = \arcsin[n_{\text{cl}} \sin(\alpha + \theta)] + \arcsin[n_{\text{cl}} \sin(\alpha - \theta)],$$

$$\theta_{\text{ext}} = \frac{1}{2} \arcsin[n_{\text{cl}} \sin(\alpha + \theta)] - \frac{1}{2} \arcsin[n_{\text{cl}} \sin(\alpha - \theta)].$$

$$(3.12)$$

Here 2α is the beam intersection angle inside the fiber, determined from the equation $\sin \alpha = (n_{\text{eff}}/n_{\text{cl}})(\lambda_{\text{uv}}/\lambda_B^0 \cos \theta)$, where n_{eff} is the effective refractive index of the bound mode for which the grating is designed. Figure 7 shows a plot of the experimental results for peak reflectivity (circles) for tilt angles up to 15° overlaid on the calculated result (line) for gratings of roughly the same strength ($2\kappa = 1.0 \times 10^{-3}$). As pointed out above, the imperfect agreement results mostly from alignment variations.

In Fig. 8(a) the experimentally measured reflectivity spectra are plotted versus tilt angle, where wavelength detuning is defined relative to the design wavelength. All gratings have a measured design wavelength of roughly but not exactly 1550 nm, since the interferometer was realigned but not recalibrated before the writing of each grating. Note that, for reasons of convenience, what is actually plotted is 1 minus the experimentally measured transmission. The 0.2-nm resolution of the optical spectrum analyzer limits the visibility of Fabry–Perot fringes like those seen in the calculated spectra of Fig. 5.
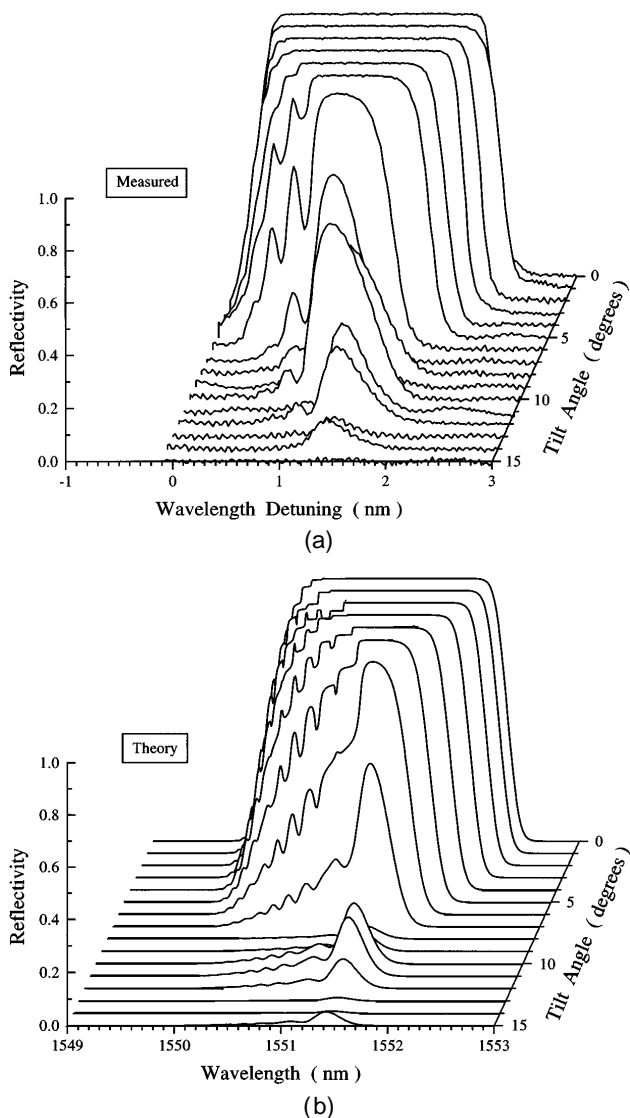

(a)

(b)

Fig. 8. (a) Experimentally measured grating reflectivity spectra versus tilt angle, (b) corresponding calculated reflectivity spectra assuming a 0.2-nm resolution-limited smoothing.
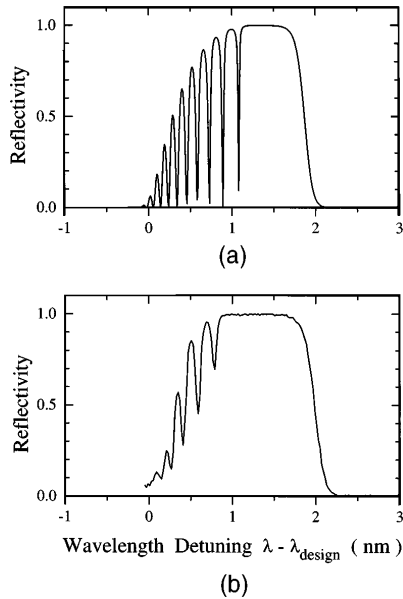
Fig. 9. Comparison of (a) the calculated reflectivity spectrum and (b) the measured reflectivity spectrum for a grating with a 5° tilt angle. No smoothing has been used on the calculated spectrum.

Therefore, in Fig. 8(b) we replot the theoretical predictions over the range 0°–15°, including smoothing that would result from a 0.2-nm-resolution measurement. The measured spectra show good qualitative agreement with calculated predictions.

A more careful comparison is made for the specific case $\theta = 5°$ in Fig. 9. Here the theoretically predicted reflectivity spectrum is plotted in Fig. 9(a), and the measured spectrum with a 0.1-nm spectrum-analyzer resolution is plotted in Fig. 9(b). Even with a higher measurement resolution, the longest-wavelength resonance (reflectivity dip) is not visible on the experimental plot. However, measurement resolution alone does not account for the disagreement between the two spectra. The number of Fabry–Perot resonances on the measured spectrum is fewer than that on the calculated spectrum. This discrepancy suggests that the actual gratings are shorter than the 5-mm FWHM used for the theoretical calculation. Good agreement on the number of Fabry–Perot resonances can be obtained by the use of 3 mm < FWHM < 4 mm for the calculation. But the calculated spectrum for FWHM < 5 mm shows a substantially less steep spectral dependence on the long-wavelength side of the spectrum than is actually measured; i.e., the steepness of the sides of the spectrum agrees best when a FWHM = 5 mm is used for the calculation. Therefore we infer that the disagreement results from the fact that the actual grating profiles are not perfectly Gaussian, as assumed for the calculation.

4. RADIATION-MODE COUPLING

The Bragg scattering treated in the last section is indicated schematically in Fig. 10(a), where along the horizontal axis we indicate the β of the discrete and radiation modes in a single-mode fiber assumed to have an infinite cladding. At shorter wavelengths [Fig. 10(b)]

the same grating can couple a forward-propagating discrete mode into backward-propagating radiation modes, resulting in the coupling of energy out of the fiber. At even shorter wavelengths or for a much longer grating period, as depicted in Fig. 10(c), a grating can couple a forward-propagating discrete mode into forward-propagating radiation modes. This last case requires a grating with a spacing much longer than the wavelength of light; we do not consider such long-period gratings here, restricting our attention to the radiation-mode coupling that short-period gratings exhibit, as in the case of Fig. 10(b).

An alternative way of looking at the various regimes of bound-mode to radiation-mode coupling is shown in Fig. 11. Here, for a given choice of grating period, the solid line represents the maximum allowed wavelength for a forward-going LP_{01} mode to couple to a backward-going radiation mode [see Fig. 10(b)]; the dotted line represents the minimum allowed wavelength for a forward-going LP_{01} mode to couple to a forward-going radiation mode [see Fig. 10(c)]; and the dashed line represents the boundary between these two cases, in
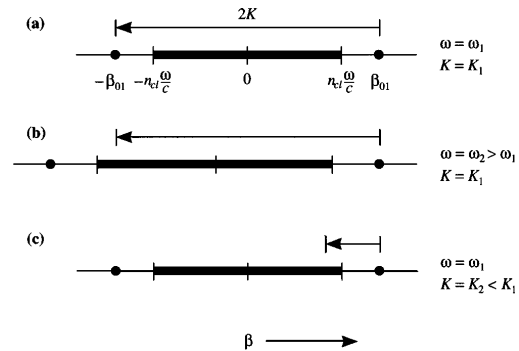

Fig. 10. Schematic illustration of three regimes of grating coupling in propagation-constant space: (a) forward bound-mode to backward bound-mode coupling, (b) forward bound-mode to backward radiation-mode coupling, (c) forward bound-mode to forward radiation-mode coupling.
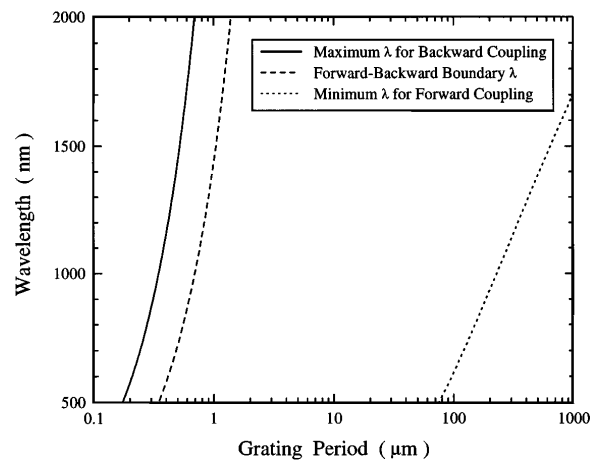

Fig. 11. Plot of the longest wavelength allowed for forward bound-mode to backward radiation-mode coupling (solid), the shortest wavelength allowed for forward bound-mode to forward radiation-mode coupling (dotted), and the boundary wavelength between forward and backward coupling (dashed), all as a function of grating period. The fiber parameters used to generate this plot are those used throughout the manuscript.

which a LP_{01} mode may couple to the radiation mode that propagates normal to the fiber axis. For a grating with a design wavelength of 1550 nm for LP_{01}-mode Bragg reflection in Corning Flexcore fiber the maximum allowed radiation-mode coupling wavelength is 1548.85 nm, and the boundary wavelength between backward- and forward-going radiation-mode coupling occurs at 776.75 nm.

In practice the situation is not as simple as that indicated in Fig. 10. For, although the nominal wave number $2K$ of the grating connects the forward-propagating discrete mode either with the backward-propagating discrete mode or with the radiation modes, in fact the broadening of the Bragg resonance that is due to the strength of the grating and the background rise in the index of refraction (see Section 3) means that the frequency regions of radiation-mode coupling and Bragg scattering can overlap; and in any case the effect of the background rise in the index of refraction leads to local modifications of the β's of both the discrete and radiation modes. What is therefore required is in fact a combined treatment of both Bragg scattering and the effects of radiation-mode coupling.

The focus of such a treatment can be on either the discrete mode or the generated radiation fields. Here our emphasis will be on the discrete mode, although the formalism developed can be used to calculate the radiated fields as well. We can anticipate that the coupled-mode equations (3.4) will be generalized to include an extinction coefficient describing the loss of energy to the radiation field. In a fiber with a finite cladding the situation is more complicated. There, for β's ranging in absolute value between ω/c and $\omega n_{cl}/c$, there exist discrete cladding modes; energy can couple from the original discrete core mode to the cladding modes and back again, leading to resonances that mimic the Bragg resonance peak.[5] This range of phenomena we defer to a later paper. The infinite-cladding geometry that we consider here is applicable, to good approximation, to a fiber dipped in index-matching fluid or recoated with an appropriate polymer coating after the grating is grown.

In our problem of interest, then, the initial state of the electromagnetic field is the discrete core mode, and the final states are the continuum of radiation modes. This bears a striking similarity to the spontaneous emission of an atom from its excited state, treated many years ago by Wigner and Weisskopff[14]; again, the initial state is discrete, with the atom in an excited state and no photons present, and the final states are a continuum, the continuum of one-photon states with the atom in its ground state. So it is not surprising that our treatment here will run parallel to the Wigner–Weisskopff analysis (although of course our problem is purely classical), with propagation along the fiber axis in our problem taking the place of evolution in time in the usual Wigner–Weisskopff analysis. In this approach the approximations involved are easily identified, the calculation is simple and, we feel, the most elegant—the radiation fields themselves tell the discrete mode that it must decay in amplitude as energy is emitted, since Maxwell's equations satisfy energy conservation.

We begin by returning to the general equations (2.21) and (2.22) and collecting the relevant (i.e., phase-matched) terms [see the comments after Eqs. (3.1)]. We use the notation (3.3) to describe the discrete modes, assuming that both forward- and backward-propagating modes will be present as a result of possible Bragg scattering. Then, despite the fact that we are in the regime indicated by Fig. 10(b), both forward- and backward-propagating radiation modes must be included. Keeping the appropriate phase-matched terms, we have

$$\bar{\beta}^{-1}\frac{\mathrm{d}a_\alpha^-}{\mathrm{d}z} = -i\kappa(z)\exp[-\tfrac{1}{2}i\phi(z)]\nu_{\alpha;01}^{-+}u(z)\exp[i(\beta-K)z],$$

$$\bar{\beta}^{-1}\frac{\mathrm{d}a_\alpha^+}{\mathrm{d}z} = i\kappa(z)\exp[\tfrac{1}{2}i\phi(z)]\mu_{\alpha;01}^{+-}v(z)\exp[-i(\beta-K)z]$$

$$(4.1)$$

for the radiation modes, where here we reserve α as a label for the radiation modes (with propagation constant β), designating the discrete mode explicitly by (01) (with propagation constant β_{01}). Adding the radiation modes that can be phase matched into Eqs. (3.1), we replace Eqs. (3.4) by

$$\bar{\beta}^{-1}\frac{\mathrm{d}u}{\mathrm{d}z} = i\gamma(z)u(z) + ig_b\kappa(z)v(z) + i\kappa(z)\exp[\tfrac{1}{2}i\phi(z)]$$

$$\times \sum_\alpha \mu_{01;\alpha}a_\alpha^-(z)\exp[i(K-\beta)z],$$

$$\bar{\beta}^{-1}\frac{\mathrm{d}v}{\mathrm{d}z} = -i\gamma(z)v(z) - ig_b\kappa(z)u(z) - i\kappa(z)\exp[-\tfrac{1}{2}i\phi(z)]$$

$$\times \sum_\alpha \nu_{01;\alpha}a_\alpha^+(z)\exp[-i(K-\beta)z], \qquad (4.2)$$

where

$$\gamma(z) \equiv g_f\sigma(z) + \delta - \tfrac{1}{2}\bar{\beta}^{-1}\frac{\mathrm{d}\phi}{\mathrm{d}z}. \qquad (4.3)$$

Consider first Eqs. (4.1). The philosophy of the calculation is that, like the Bragg scattering, the radiation-mode coupling will affect the amplitudes $u(z)$ and $v(z)$ only over distances that are much greater than $\bar{\beta}^{-1}$. Thus, with respect to solving Eqs. (4.1), over distances of the order of a few $\bar{\beta}^{-1}$ from $z = z_0$, we may write

$$u(z) \approx u(z_0)\exp[i\bar{\beta}\gamma_0(z-z_0)],$$

$$v(z) \approx v(z_0)\exp[-i\bar{\beta}\gamma_0(z-z_0)],$$

$$\phi(z) \approx \phi(z_0) + \left(\frac{\mathrm{d}\phi}{\mathrm{d}z}\right)_0(z-z_0), \qquad (4.4)$$

where $\gamma_0 \equiv \gamma(z_0)$. Using relations (4.4) in Eqs. (4.1), we can find the particular solution for $a_\alpha^\pm$. Then, using relations (4.4) again, we can regroup the terms to find, for example for a_α^-,

$$a_\alpha^-(z) = \frac{-\bar{\beta}\kappa(z)\exp[-\tfrac{1}{2}i\phi(z)]\exp[i(\beta-K)z]\nu_{\alpha;01}^{-+}u(z)}{\beta-\beta_{res}(z)},$$

$$(4.5)$$

where

$$\beta_{res}(z) \equiv K - \bar{\beta}\gamma(z) + \frac{1}{2}\frac{\mathrm{d}\phi}{\mathrm{d}z}. \qquad (4.6)$$

Using Eq. (4.5) and the corresponding equation for a_α^+ in Eqs. (4.2), we find that

$$\bar{\beta}^{-1}\frac{\mathrm{d}u}{\mathrm{d}z} = [i\gamma(z) - \kappa^2(z)A(z)]u(z) + ig_b\kappa(z)v(z),$$

$$\bar{\beta}^{-1}\frac{\mathrm{d}v}{\mathrm{d}z} = -[i\gamma(z) - \kappa^2(z)A(z)]v(z) - ig_b\kappa(z)u(z), \quad (4.7)$$

where

$$A(z) = i\bar{\beta}\sum_{\rho p}\frac{|\nu_{\rho p;01}^{-+}|^2}{\beta - \beta_{\mathrm{res}}(z)}, \quad (4.8)$$

and we now explicitly show α as consisting of the parameter ρ labeling the continuous modes [Eq. (2.9)] and an index p indicating other degeneracies [cf. Eq. (2.11)]. In writing Eq. (4.8), we have used the fact that

$$\mu_{01;\rho p}^{+-}\nu_{\rho p;01}^{-+} = |\nu_{\rho p;01}^{-+}|^2 \quad (4.9)$$

[see Eqs. (2.26) and (2.27)].

The sum over ρ in Eq. (4.8) is really an integral, which we exhibit below converted [using Eq. (2.9)] to an integral over β. The β in the denominator of Eq. (4.8) is the propagation constant associated with the radiation mode labeled by ρ. To be able to perform the resulting integral subject to the boundary condition of outgoing radiation fields, we replace in the usual way β by $\beta + i\epsilon$, where ϵ is a small positive number. This gives us the expression

$$A(z) = i\bar{\beta}\sum_p \int \frac{\beta\,\mathrm{d}\beta}{\rho}\frac{|\nu_{\rho p;01}^{-+}|^2}{\beta + i\epsilon - \beta_{\mathrm{res}}(z)}, \quad (4.10)$$

which we evaluate using the expression

$$\frac{1}{\beta + i\epsilon - \beta_{\mathrm{res}}(z)} \to \mathcal{P}\left[\frac{1}{\beta - \beta_{\mathrm{res}}(z)}\right] - i\pi\delta[\beta - \beta_{\mathrm{res}}(z)], \quad (4.11)$$

where the first term on the right-hand side of relation (4.11) indicates the principal part. That term makes a contribution to $A(z)$, which, when inserted back in Eqs. (4.7), leads to a small shift in the effective detuning. This term, analogous to the Lamb shift in the Wigner–Weiskopff analysis, we neglect. It is the Dirac delta function term in relation (4.11) that leads to the physically new effect, the decay of the discrete mode amplitude on account of radiation, and using it in Eq. (4.10), we find that

$$A(z) = \sum_p\left(\frac{\beta\pi}{\rho}\bar{\beta}|\nu_{\rho p;01}^{-+}|^2\right)_{\beta=\beta_{\mathrm{res}}(z)}$$

$$\equiv \sum_p A_p(z), \quad (4.12)$$

which is positive and real. Returning to Eqs. (4.7), we can now identify $A(z)$ as an effective extinction coefficient for the discrete mode and $A_p(z)$ as the contribution to it from the modes of degeneracy index p.

Note that the only dependence of $A(z)$ on position is through its dependence on $\beta_{\mathrm{res}}(z)$ on position. Using Eqs. (3.5) and (4.3) in Eq. (4.6), we find that

$$\beta_{\mathrm{res}}(z) = \left(2K + \frac{\mathrm{d}\phi}{\mathrm{d}z}\right) - [\beta_{01} + \bar{\beta}g_f\sigma(z)]. \quad (4.13)$$

The term in large parentheses on the right-hand side of Eq. (4.13) is the local wave number of the grating, taking into account its possible chirp, and the term in square brackets is the local propagation constant of the discrete mode, taking into account its modification that is due to the background induced index. Thus $\beta_{\mathrm{res}}(z)$ gives the local version of the resonance condition sketched in Fig. 10(b) for the radiation mode, as might be expected. Field amplitudes $u(z)$ and $v(z)$ satisfying Eqs. (4.7) no longer satisfy the energy conservation condition (3.11). Instead, it is easy to confirm that they satisfy

$$\frac{\mathrm{d}}{\mathrm{d}z}[|u(z)|^2 - |v(z)|^2] = -2\bar{\beta}\kappa^2(z)A(z)[|u(z)|^2 - |v(z)|^2], \quad (4.14)$$

showing that the flux of light through the fiber decreases along the direction of energy propagation on account of scattering of light out into the radiation modes. Clearly Eqs. (4.7) and (4.14) describe this loss in a local approximation, which entered the derivation through the approximate Eq. (4.5). We turn to a discussion of its range of validity in Section 7.

5. EXTINCTION COEFFICIENTS

In this section we consider the extinction coefficients A and A_p of Eq. (4.12); these depend on z only through the dependence of β_{res} on z, so we will consider them as a function of β. Returning to Fig. 1, we note that a bound LP_{01} mode can be either s- or p-polarized with respect to the grating, and we can consider coupling to radiation modes that are either s- or p-polarized with respect to the grating. For a radiation mode of type LP_q, $q = 0, 1, 2, \ldots$, then, there are four coefficients to consider: $A_q^{j\leftarrow i}$, as i and j vary over s and p. Using in Eq. (4.12) the well-known[9] expressions for the bound and radiation modes in the LP approximation, we can put the extinction coefficients in the form

$$A_q^{j\leftarrow i} = \frac{4(\beta a)^2(\rho a)^{2q}b_{01}}{\pi e_q J_1^2(\kappa_{01}a)\Gamma_q}|c_q^{j\leftarrow i}|^2, \quad (5.1)$$

where $e_q = 2$ if $q = 0$, and $e_q = 1$ otherwise, ρ is as defined in Eq. (2.9), and

$$\Gamma_q \equiv [\tau a(\rho a)^q J_{q+1}(\tau a)J_q(\rho a) - (\rho a)^{q+1}J_q(\tau a)J_{q+1}(\rho a)]^2$$
$$+ [\tau a(\rho a)^q J_{q+1}(\tau a)N_q(\rho a)$$
$$- (\rho a)^{q+1}J_q(\tau a)N_{q+1}(\rho a)]^2, \quad (5.2)$$

with

$$\tau \equiv \sqrt{n_{\mathrm{core}}^2 k^2 - \beta^2} \quad (5.3)$$

and where N_q is the Bessel function of the second kind of order q. The terms $c_q^{j\leftarrow i}$ appearing in Eq. (5.1) are integrals of products of Bessel functions over the core.
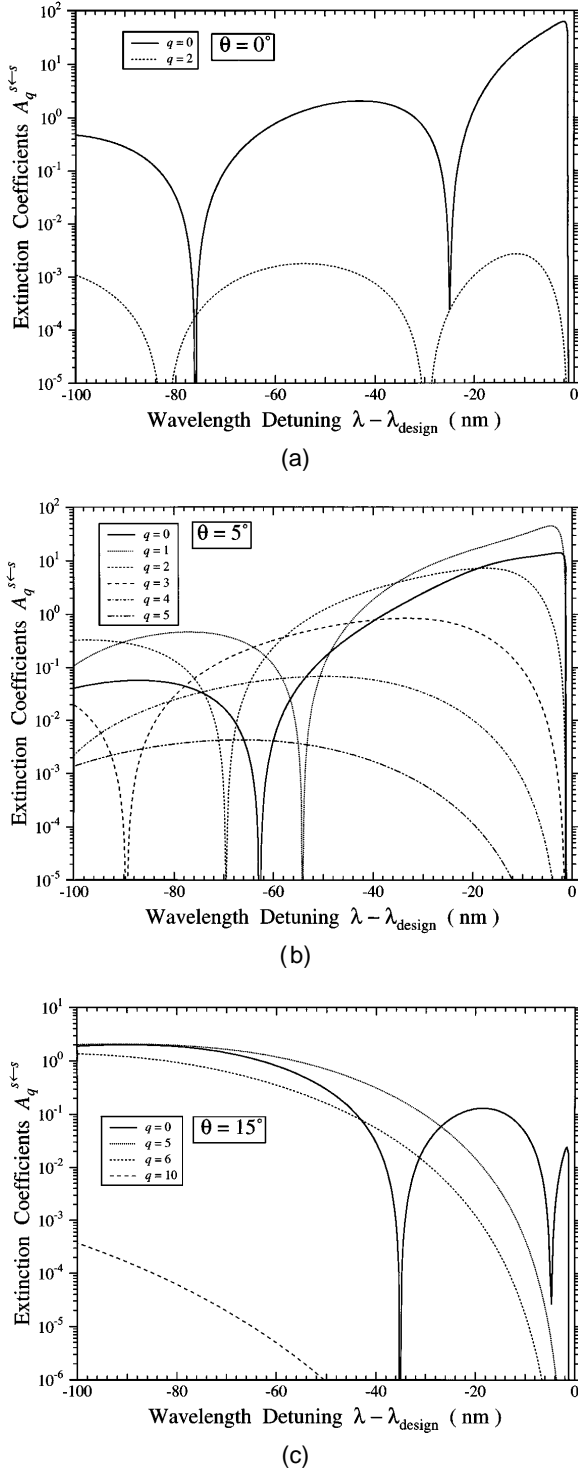
(a)

(b)

(c)

Fig. 12. Calculated extinction coefficients for s-polarized bound-mode to s-polarized LP_q radiation-mode coupling. Plots are made for grating tilt angles of (a) 0°, (b) 5°, and (c) 15°.

Expressions for them are given in Appendix B; in general they must be evaluated numerically.

In order to provide a better understanding of the characteristics of the extinction coefficients A_q, we plot some examples in Fig. 12. Figure 12(a) shows the extinction coefficients for an untilted grating ($\theta = 0°$) for $s \leftarrow s$ polarization coupling. The grating is assumed to have identical parameters to those used for Figs. 4 and 5,

with $2\kappa = 1.0 \times 10^{-3}$. For an untilted grating the only nonzero coefficients occur for $q = 0$ and 2. In Fig. 12(b) the coefficients for $q = 0$ through 5 and $s \leftarrow s$ coupling are plotted for a grating with a tilt of $\theta = 5°$. The important point to note in this plot is that the $q = 5$ coefficient is several orders of magnitude smaller than the dominant coefficients over the entire wavelength range investigated, suggesting that a calculation including only the coefficients for $q \leq 5$ provides an accurate estimate of the radiation-mode coupling strength for a grating with $\theta = 5°$. In Fig. 12(c) the coefficients for $q = 0$, 5, 6, and 10 are plotted for a grating with a tilt of $\theta = 15°$. The plot shows that including coefficients as high as $q = 10$ is not necessary when $\theta = 15°$, but by including only $q \leq 5$, one somewhat underestimates the total coupling loss at wavelengths well below the design wavelength, as the $q = 6$ coefficient is nearly as large as the dominant coefficients. At even higher tilt angles larger q values should be included for an accurate representation of the coupling loss.

We note that for all of the tilt angles discussed here the $p \leftarrow p$ extinction coefficients are similar to the $s \leftarrow s$ coefficients but with slightly different spectral shape and slightly smaller magnitude. A more careful comparison between these two kinds of coupling will be made in Section 6, wherein we look at the calculated transmission loss spectrum. The $s \leftarrow p$ and $p \leftarrow s$ coefficients are smaller than either the $s \leftarrow s$ or $p \leftarrow p$ coefficients by several orders of magnitude. Hence we neglect these dissimilar polarization extinction coefficients in the transmission loss calculations of the next section.

6. FIBER SPECTRA

In this section we compare experimental results with theoretical calculations based on the coupled-mode equations (4.7), using extinction coefficients $A(z)$ evaluated as discussed in the previous section.

These equations must be solved numerically through the fiber profile. The calculation is more complicated than that described in Section 3 because we must evaluate the integrals in Appendix B at each point in the fiber profile to calculate $A(z)$. To simplify the computations, we make a number of approximations that do not significantly affect the results. First, in calculating the contributions to $A(z)$, we neglect the contributions from the z component of the bound mode and do not calculate the depolarized scattering, calculating either $s \leftarrow s$ or $p \leftarrow p$ scattering only. The first approximation eliminates the terms in Eqs. (B2) and (B4) involving the factor $\kappa_{01}\rho/\beta_{01}\beta$, so there are only three integrals left to evaluate. In evaluating these integrals, we approximate $\kappa_{01}a$ by its value at the design wavelength. Then, once $\kappa_{01}a$ and $2Ka \tan \theta$ are specified, the three integrals must be evaluated only as a function of τa; this can be done before the integration of the coupled-mode equations through the grating profile, and the values of $A(z)$ then essentially read from a table as the integration is performed. As in Section 3, we evaluate g_b and g_f at the design wavelength, and, although in expression (3.5) for δ we make the approximation

$$\delta \approx \frac{\beta_{01} - K}{K},$$
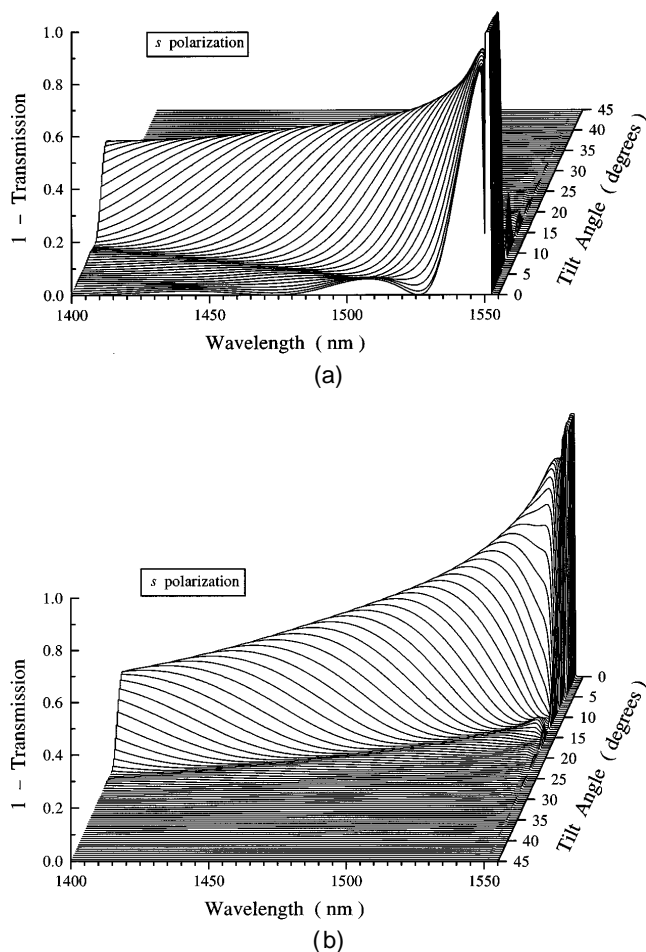
(a)

(b)

Fig. 13.   Calculated transmission loss spectra versus grating tilt angle for s-polarized bound-mode to s-polarized bound-mode and radiation-mode coupling, where all LP$_q$ radiation modes for $q \leq 5$ have been included.   The waterfall of spectra is plotted in both (a) ascending and (b) descending order of tilt angle.

we do evaluate β_{01} at each frequency.   Over the range of frequencies and grating angles in which we are interested these approximations are certainly adequate and considerably shorten the calculation.

Figure 13 shows calculated transmission spectra (plotted as 1 minus transmission for viewing clarity) versus grating tilt angle for s-polarized light, where both Bragg reflection and bound-mode to radiation-mode coupling loss are included.   The fiber and grating parameters assumed for this plot are identical to those used for Figs. 4 and 5, and the grating amplitude is $2\kappa = 1.0 \times 10^{-3}$.   The waterfall of spectra is plotted in both (a) ascending and (b) descending order of tilt angle.   Note that the longest wavelength loss peak in each spectrum is due almost exclusively to Bragg reflection loss (cf. Fig. 5), whereas the remainder of each spectrum is due to radiation-mode coupling loss; however, the two contributions overlap in the vicinity of the design wavelength (1550 nm).   For this calculation the summation in Eq. (4.12) included radiation modes with azimuthal quantum numbers ranging from 0 to 5; for a given bound-mode polarization (s in this case), only coupling to the like-polarized radiation mode was considered. We observed that the spectra do not change drastically when higher-azimuthal-order

radiation modes and the dissimilar radiation-mode polarization are included.   The changes are insignificant for the smaller tilt angles ($\theta < 15°$).   Figure 14 shows a similar calculation for the case of p-polarized bound-mode to p-polarized radiation-mode coupling.

In contrast to the case of Bragg reflection from a tilted grating (Section 3), for bound-mode coupling to radiation modes the s- and p-polarized cases behave quite differently—in all cases the p-polarized bound mode sees less radiation-mode coupling loss than the s-polarized mode. To examine this difference more closely, in Fig. 15 we plot the calculated absolute minimum transmission (maximum loss) versus grating tilt angle for both s-polarized (solid) and p-polarized (dotted) bound-mode to radiation-mode coupling.   For this fiber the two polarizations scatter quite similarly for tilt angles less than approximately 6.5°; above this tilt angle p polarization begins to scatter less efficiently than s polarization.   The origin of the kink in these curves at a 6.5° tilt angle is clear from Figs. 13(b) and 14(b)—for tilt angles smaller than 6.5° the minimum transmission derives from the narrow peak on the long-wavelength side of the radiation-mode loss spectrum; for larger tilt angles the minimum transmission is determined by the broader peak at shorter wavelengths.   The different rates of change of transmission with tilt angle associated with these two peaks thus give rise to the kinks in Fig. 15.   We note that in the vicinity of 6.5° tilt angle
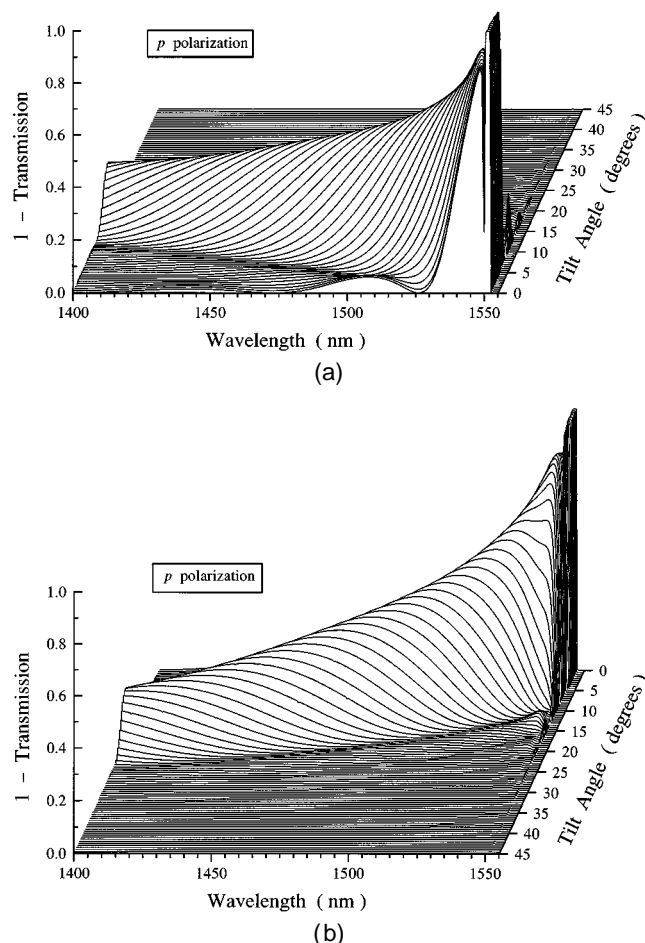

(a)

(b)

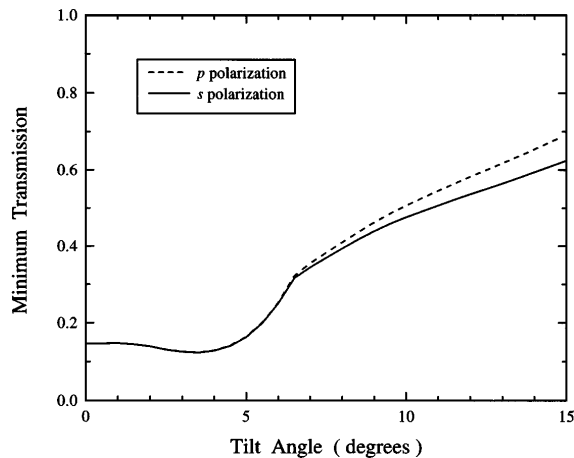Fig. 14.   Same as Fig. 13, but for p polarization.

Fig. 15. Calculated absolute minimum transmission (maximum loss) that is due solely to radiation-mode coupling for s-polarized bound-mode to s-polarized radiation-mode coupling (solid) and for p-polarized coupling (dashed).

for this fiber the narrow peak on the long-wavelength side is caused by scattering into even-azimuthal-order radiation modes, whereas the broader peak results from scattering into odd-azimuthal-order radiation modes.

For a comparison of the calculated results with experimental results the transmission spectra of the same set of gratings described in Section 3 were measured over the wavelength range of interest for bound-mode to radiation-mode coupling. For these measurements the bare (uncoated) fiber was immersed in index-matching fluid with a cladding-fluid index difference of less than 0.01. This difference was suitable to remove any detectable evidence of resonances associated with coupling between the LP_{01} bound mode and cladding modes. When glycerin was used for index matching, the transmission curves exhibited a slight ripple (less than 10% of the transmission) at the longest wavelengths, caused by non-total-internal-reflection Fresnel reflections of the radiation modes off the cladding−glycerin interface. The ripple increased somewhat when the grating region of the bare fiber was recoated with a higher index uv-curable polymer coating.

The measured transmission spectra are plotted in Fig. 16(a), where wavelength detuning is defined relative to the measured design wavelength. For convenience the theoretical predictions are replotted in Fig. 16(b) over the range of tilt angles experimentally measured. There is reasonably good agreement between the measured and calculated spectra. As pointed out in Section 3, because of variations in actual uv-induced index change and index modulation resulting from changes in the alignment from grating to grating, the most accurate comparison of the spectra in Fig. 16 with each other and with calculations should be based on spectral shape rather than actual values of transmission. For example, Fig. 17 shows that there is good agreement of the measured wavelengths of minimum transmission (circles) versus tilt angle with the calculated wavelengths (line). Furthermore, it is comforting to note that the peak responsible for maximum loss switches from the narrow, long-wavelength peak in the 6° tilt spectrum to the broader, shorter-wavelength peak at 7° tilt, just as predicted by the theory. However, the measured spectra in Fig. 16 tend to exhibit a larger

ratio of loss in the side peaks to that in the main peak [cf. Figs. 13, 14, and 16(b)]. Furthermore, the measured spectra for the highest tilt angles (13°−15°) appear to
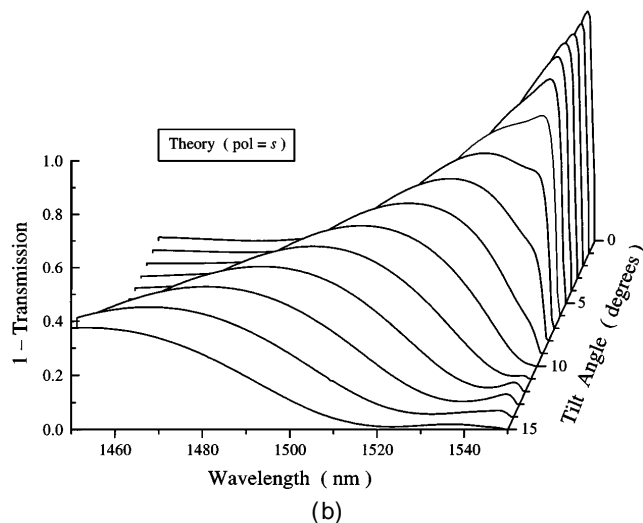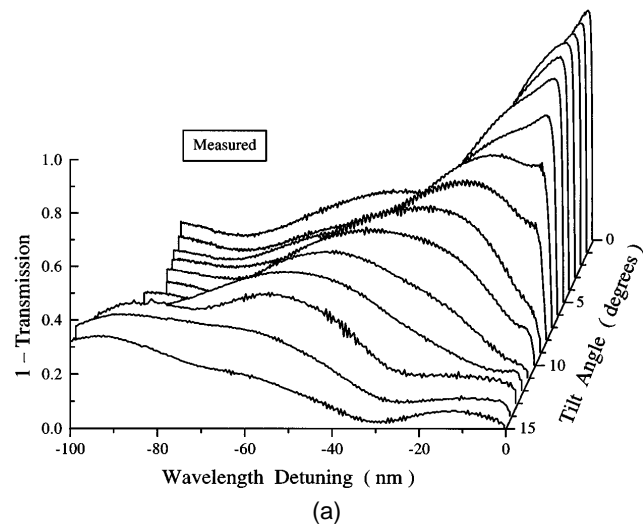

(a)

(b)

Fig. 16. (a) Experimentally measured transmission loss spectra versus grating tilt angle for gratings written with tilt angles of 0°−15°, (b) corresponding calculated transmission loss spectra, where loss that is due to Bragg scattering has been excluded.
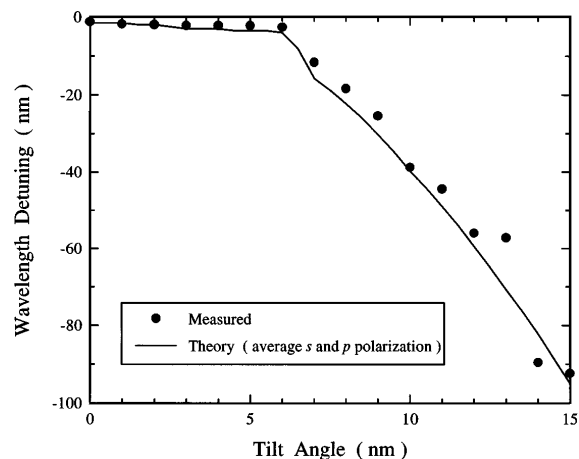

Fig. 17. Measured wavelength of minimum transmission (circles) and calculated wavelength of minimum transmission (solid) versus tilt angle, where loss that is due to Bragg scattering has been excluded.

have one more peak over the wavelength range measured than predicted by the theory [cf. Figs. 13(b), 14(b), and 16(b)].

7. CONCLUSIONS

Throughout the preceding sections the agreement between theory and experiment has been not only qualitatively good but in many cases quantitatively good as well. In this section we review the approximations that enter the theoretical description and the difficulties that affect the experimental results; the goal is not only to uncover the sources of the discrepancies in this work but also to identify sources of discrepancies that would plague experiments in other regions of parameter space.

Of the theoretical approximations, many seem clearly adequate. The small uv-induced changes in the index of refraction involved here completely justify the approximation of Eqs. (2.15) by relation (2.16), for example. Likewise, one would naively expect that the neglect of the higher-order Fourier components [discussed after Eq. (2.18) and before Eqs. (3.2)] is harmless; an indication of how large the induced index change would have to be to necessitate a more detailed calculation can be gleaned from the analysis presented by Sipe *et al.* in Ref. 10.

That analysis, however, and others like it rely on treating the propagating fields as essentially one dimensional in nature. A qualitatively different effect arises when the index changes in the core, although leading to small grating amplitudes, are large enough that the average core index change, although small, allows the fiber to support a new bound mode. Then the expansion in Eq. (2.11), although mathematically correct in that the modes of the unperturbed fiber form an essentially complete set, is no longer physically reasonable in that the approximations made following that expansion are no longer appropriate. This is a matter to which we plan to turn in a future paper; but with respect to this work it is irrelevant, since the index changes are not large enough to lead to new bound modes. We note in passing that leaky modes are of course linear combinations of radiation modes[9] and as such are implicit in our calculation.

Turning specifically to the radiation-mode coupling, we note that the description presented here of the extinction of a bound mode as a result of that coupling is within a local approximation [see the comment after Eq. (4.14)]; in the language of the Wigner–Weisskopf calculation the extinction coefficient is essentially a local Fermi's golden rule result. The validity of this calculation then follows from the usual discussion of the validity of Fermi's golden rule.[15] The length L over which the grating parameters change significantly must satisfy $L > \sim 1/\Delta\beta$, where $\Delta\beta$ is the wave-number range over which nonnegligible quantities $(\beta\pi/\rho)\bar{\beta}|\nu_{\rho p;01}^{-+}|^2$ vary significantly from their values at β_{res} [see Eq. (4.12)]. For the grating and fiber parameters involved in the work of this paper this condition is well satisfied.

A more general approximation is that of using the LP mode description with the assumption of a step-index profile. Although we have not made a detailed study of limitations that are due to the LP mode approximation, for the small core-cladding difference in the Corning Flexcore fiber [see the discussion after Eq. (3.10)] we feel that this

is hardly the most serious limitation of this work. It is true that we neglect the z components of the bound-mode field; but because the z components of the radiation-mode fields are kept, that approximation should be valid for the fiber considered here, regardless of tilt angle and detuning from the design wavelength.

The step-index profile assumption is perhaps more serious; although we have not made a detailed study of this assumption, simple arguments indicate that if it limits the accuracy of our theoretical predictions, it is at the larger detunings from Bragg scattering. This may be one reason for the slight disagreement between theory and experiment in the shape and the magnitude of the spectra in Fig. 16 for wavelengths well below the design wavelength.

Another possible culprit responsible for this slight disagreement at large detunings from the design wavelength is the neglect of radiation-mode azimuthal orders $q > 5$ in the calculations presented in Section 6. However, a set of calculations not presented here indicates that the influence of radiation-mode azimuthal orders $q > 5$ is qualitatively significant only for tilt angles greater than approximately 15°; such large tilt angles are not considered here experimentally but might be of interest for some applications.

Finally, we discuss possible experimental causes of disagreement between calculated and measured results for both Bragg scattering and radiation-mode loss. A main limitation of the experimental accuracy is the fact that the entire interferometer alignment was changed between the writing of each grating. We could not just rotate the fiber in 1° increments, because that would lead to design wavelengths that vary over a range of ~ 150 nm for tilt angles varying from 0° to 15°. Therefore, the zero-tilt design wavelength (i.e., the uv beam intersection angle) was changed after each exposure, so that the actual design wavelength would be roughly 1550 nm for all of the gratings, regardless of tilt angle. After an alteration of the interferometer as significant as this, a recalibration of exposure conditions and wavelength is usually required to yield reproducible results. Recalibration entails writing multiple gratings, renormalizing exposure time and intensity, and adjusting the uv writing wavelength. Since such a recalibration was not done between each tile exposure, two important effects occur, as detailed below.

First, the uv-induced index change is likely not the same for all of the measured gratings, as is certainly assumed in the theoretical plots. A large variation in induced index change would occur on account of alignment variations if simply equal exposure times were used. Therefore an attempt was made to attain more equal index change through real-time monitoring of the transmission spectra during growth and accordingly through adjusting the exposure times. Nevertheless, the index change still probably has a substantial variation from grating to grating, and we feel that this variation is largely responsible for the disagreement between theory and experiment. This disagreement is particularly noticeable in the reflectivity spectra (Figs. 7 and 8).

Second, the grating fringe visibility (the ratio $2\kappa/\sigma$) is likely not the same for all of the measured gratings; perfect visibility ($2\kappa/\sigma = 1$) is assumed for all of the calculations. Thermal and vibrational instabilities in the interferometer cause this variation. The settling time and

the environmental conditions varied before the writing of each grating, giving rise to a variation in the visibility. A rough estimate is that the visibility could vary by as much as $\pm 10\%$.

In addition to the experimental grating-to-grating variations just described, it is also possible that the geometry used to provide the grating tilt could explain some of the discrepancy between the theory and the measurements. One explanation might be that the focal planes of the two uv beams are not parallel to the fiber axis for a tilted grating. However, even for a 30° grating tilt angle (for which $\theta_{\text{ext}} = 50°$ and $\alpha_{\text{ext}} = 20°$), the fiber does not deviate from the focal plane by more than 10% of the Rayleigh range for the beam size and the cylindrical lens used. This deviation implies an intensity variation from that at the focal plane of less than 1% and a corresponding negligible variation in fringe visibility of less than 10^{-4}.

A second, more plausible geometric explanation of the discrepancy might be that the fringe visibility of the interference pattern formed by the intersection of the two nonuniform (Gaussian) uv beams varies along an axis tilted with respect to the normal to the bisector of the two beams. If the two beams have equal intensity, the visibility is perfect (=1) at the center of the grating but then diminishes away from the center along the tilted fiber axis as a result of the different projected widths of the two Gaussian beams on the fiber. One beam will have a projected width of FWHM/$\cos(\alpha_{\text{ext}} + \theta_{\text{ext}})$, and the other will have a width of FWHM/$\cos(\alpha_{\text{ext}} - \theta_{\text{ext}})$, where FWHM is the transverse full width at half-maximum of the beam. Again, when we consider the severe case of $\theta = 30°$, the visibility will drop only by approximately 3% a distance of FWHM/2 away from the grating center along the fiber axis. Nevertheless, the visibility will drop more rapidly farther out, giving rise to a non-Gaussian profile of the index modulation parameter 2κ and an effectively shorter grating length than would occur for zero tilt. These two effects were observed and are discussed in Section 3, wherein the experimental and theoretical reflection spectra are compared for a grating with a 5° tilt angle. It is not clear that this geometric explanation is a primary cause of theory–measurement discrepancy, though.

In summary, then, although there are theoretical limitations of the description that we have presented that could affect experiments for other grating and fiber parameters, the main source of disagreement between theory and experiment in the present study appears to be the experimental difficulty in controlling the parameters of the gratings actually written. Nevertheless, the good qualitative agreement obtained is evidence that the theoretical development presented here is a valuable tool for the design of fiber-grating devices that utilize radiation-mode coupling loss for filtering applications.

APPENDIX A

In this appendix we sketch the derivation of the result (2.10)–(2.12) for the field generated by an arbitrary source polarization $\mathbf{P}(\mathbf{R})$. To begin, we find it useful to have an explicit notation for the portions of the electromagnetic field consisting of modes going to the right $(+z)$ and the left $(-z)$ in an ideal fiber in the absence of any such source polarization. We put

$$F^{\pm}(x, y, z) = \begin{pmatrix} E^{\pm z}(x, y, z) \\ H^{\pm z}(x, y, z) \\ \mathbf{E}^{\pm t}(x, y, z) \\ \mathbf{H}^{\pm t}(x, y, z) \end{pmatrix}, \qquad \text{(A1)}$$

with

$$
\begin{aligned}
F^{\pm}(x, y, z) &= \sum_{\alpha p} \tilde{a}_{\alpha p}^{\pm} f_{\alpha p}^{\pm}(x, y) \exp(\pm i\beta_\alpha z) \\
&\equiv \sum_{mp} \tilde{a}_{mp}^{\pm} f_{mp}^{\pm}(x, y) \exp(\pm i\beta_m z) \\
&\quad + \sum_p \int d\rho\, \tilde{a}_{\rho p}^{\pm} f_{\rho p}^{\pm}(x, y) \exp[\pm i\beta(\rho)z],
\end{aligned}
$$
$$\text{(A2)}$$

where the $\tilde{a}_{\alpha p}^{\pm}$ are expansion coefficients. The electric and magnetic fields appearing in Eq. (A1) satisfy the Maxwell equations

$$\nabla \times \mathbf{E}^{\pm}(\mathbf{R}) - i\omega\mu_0\mathbf{H}^{\pm}(\mathbf{R}) = 0\,,$$
$$\nabla \times \mathbf{H}^{\pm}(\mathbf{R}) + i\omega\epsilon_0 n_0{}^2(x, y)\mathbf{E}^{\pm}(\mathbf{R}) = 0\,, \qquad \text{(A3)}$$

since they consist of ideal fiber modes.

Now consider the introduction of a source polarization, but initially one confined to lie only in the $z = z'$ plane,

$$\mathbf{P}(\mathbf{R}) = \mathbf{p}(x, y)\delta(z - z')\,,$$
$$\mathbf{p}(x, y) = \mathbf{p}^t(x, y) + \hat{z}p^z(x, y)\,, \qquad \text{(A4)}$$

where we use the vector component notation of Eq. (2.2). With this expression for the source polarization the Maxwell equations now take the form

$$\nabla \times \mathbf{E}(\mathbf{R}) - i\omega\mu_0\mathbf{H}(\mathbf{R}) = 0\,,$$
$$\nabla \times \mathbf{H}(\mathbf{R}) + i\omega\epsilon_0 n_0{}^2(x, y)\mathbf{E}(\mathbf{R}) = -i\omega\mathbf{P}(\mathbf{R})\,. \qquad \text{(A5)}$$

Since there is no source polarization to the left or the right of $z = z'$, we are led to seek a solution of the form

$$
\begin{aligned}
\mathbf{E}(\mathbf{R}) &= \theta(z - z')\mathbf{E}^+(\mathbf{R}) + \theta(z' - z)\mathbf{E}^-(\mathbf{R}) \\
&\quad + \delta(z - z')\hat{z}E^d(x, y)\,, \\
\mathbf{H}(\mathbf{R}) &= \theta(z - z')\mathbf{H}^+(\mathbf{R}) + \theta(z' - z)\mathbf{H}^-(\mathbf{R})\,, \qquad \text{(A6)}
\end{aligned}
$$

where $\theta(z)$ is the unit step function, vanishing for $z < 0$ and equal to unity for $z > 0$; the expansion coefficients [see Eq. (A2)] and $E^d(x, y)$ (which, as will presently become clear, is a required part of the solution) are to be determined. Substituting Eqs. (A4) and (A6) into the Maxwell equations (A5), using

$$\nabla\theta(z - z') = \hat{z}\delta(z - z')\,,$$
$$\nabla\delta(z - z') \times \hat{z} = 0\,, \qquad \text{(A7)}$$

and Eqs. (A3), we find we must have

$$
\begin{aligned}
\hat{z} &\times [\mathbf{E}^+(x, y, z') - \mathbf{E}^-(x, y, z')] \\
&\qquad\qquad - \hat{z} \times \nabla E^d(x, y) = 0\,, \\
\hat{z} &\times [\mathbf{H}^+(x, y, z') - \mathbf{H}^-(x, y, z')] \\
&\qquad + i\omega\epsilon_0 n_0{}^2(x, y)\hat{z}E^d(x, y) = -i\omega\mathbf{p}(x, y)\,. \quad \text{(A8)}
\end{aligned}
$$

These are the discontinuity conditions imposed by the source polarization (A4). From the z component of the second of Eqs. (A8) we find that

$$E^d(x, y) = \frac{-p^z(x, y)}{\epsilon_0 n_0^2(x, y)}.$$ (A9)

Now we dot the first of Eqs. (A8) into the transverse component of the magnetic field of the (α, p) mode and the second of those equations into the associated transverse component of the electric field. Interchanging the dot and cross products and integrating over the $x-y$ plane, we find, using the expansion (A2) and the mode orthogonality conditions (2.6)–(2.8), that the mode expansion coefficients must satisfy

$$\frac{1}{2}P_{\alpha p}[\tilde{a}_{\alpha p}^+ \exp(i\beta_\alpha z') + \tilde{a}_{\alpha p}^- \exp(-i\beta_\alpha z')]$$
$$= i\omega \int \mathbf{p}^t(x, y) \cdot \mathbf{e}_{\alpha p}^{t*}(x, y)\mathrm{d}s,$$

$$\frac{1}{2}P_{\alpha p}[\tilde{a}_{\alpha p}^+ \exp(i\beta_\alpha z') - \tilde{a}_{\alpha p}^- \exp(-i\beta_\alpha z')]$$
$$= i\omega \int p^z(x, y)e_{\alpha p}^{z*}(x, y)\mathrm{d}s.$$ (A10)

The first and second of these equations follow, respectively, from the first and second of Eqs. (A8). By adding and subtracting Eqs. (A10), we can immediately recover expressions for the mode expansion coefficients,

$$\tilde{a}_{\alpha p}^+ = \frac{i\omega}{P_{\alpha p}} \exp(-i\beta_\alpha z') \int \mathbf{p}(x, y) \cdot \tilde{\mathbf{E}}_{\alpha p}^{+*}(x, y)\mathrm{d}s,$$

$$\tilde{a}_{\alpha p}^- = \frac{i\omega}{P_{\alpha p}} \exp(i\beta_\alpha z') \int \mathbf{p}(x, y) \cdot \tilde{\mathbf{E}}_{\alpha p}^{+*}(x, y)\mathrm{d}s,$$ (A11)

where we have used the mode expressions (2.4) and (2.5) to simplify the right-hand sides of Eqs. (A11).

With these results in hand we can turn to the problem of a general source polarization, which can be written in the form

$$\mathbf{P}(\mathbf{R}) = \mathbf{P}(x, y, z) = \int \mathbf{P}(x, y, z')\delta(z - z')\mathrm{d}z'.$$ (A12)

This displays such a general source polarization as just a superposition of sources of the form (A4) for different z'; thus the solution follows immediately from what we have already done by superposition. One part of the field is given by Eq. (2.10) [cf. Eq. (A9)], and the rest can be written as a superposition of modes of the ideal fiber (2.11) but with amplitudes given by

$$\tilde{a}_{\alpha p}^+(z) = \frac{i\omega}{P_{\alpha p}} \int_{-\infty}^{z} \int \exp(-i\beta_\alpha z')\mathbf{P}(x, y, z')$$
$$\cdot \mathbf{E}_{\alpha p}^{+*}(x, y)\mathrm{d}s\mathrm{d}z',$$

$$\tilde{a}_{\alpha p}^-(z) = \frac{i\omega}{P_{\alpha p}} \int_{z}^{\infty} \int \exp(i\beta_\alpha z')\mathbf{P}(x, y, z')$$
$$\cdot \mathbf{E}_{\alpha p}^{-*}(x, y)\mathrm{d}s\mathrm{d}z',$$ (A13)

[cf. Eqs. A11)], with the inner integrals ranging over the $x-y$ plane. Equations (2.12) are then obtained by differentiation of Eqs. (A13).

APPENDIX B

In this appendix we give expressions for the coefficients $c_q^{j\leftarrow i}$ appearing in Eq. (5.1). They are all of the form

$$c_q^{j\leftarrow i} = \frac{1}{2(\kappa_{01}a)^2} \int_0^{\kappa_{01}a} I_q^{j\leftarrow i}(u)u \, \mathrm{d}u,$$ (B1)

where

$$I_q^{s\leftarrow s}(u) = 2\left(\frac{n_{\mathrm{core}}k}{\beta} + 1\right)J_q(Tu)J_0(u)J_q(\Omega u)$$
$$+ \left(\frac{n_{\mathrm{core}}k}{\beta} - 1\right)[J_{q+2}(Tu)J_0(u)J_{q+2}(\Omega u)$$
$$+ J_{q-2}(Tu)J_0(u)J_{q-2}(\Omega u)]$$
$$- \frac{\kappa_{01}\rho}{\beta_{01}\beta}\{J_{q+1}(Tu)J_1(u)[J_q(\Omega u) + J_{q+2}(\Omega u)]$$
$$- J_{q-1}(Tu)J_1(u)[J_q(\Omega u) + J_{q-2}(\Omega u)]\}$$ (B2)

is the integrand involved in calculating the coupling of a LP$_{01}$ mode that is s-polarized with respect to the grating to an s-polarized LP$_q$ radiation mode. Similarly

$$I_q^{p\leftarrow s}(u) = \left(\frac{n_{\mathrm{core}}k}{\beta} - 1\right)[J_{q+2}(Tu)J_0(u)J_{q+2}(\Omega u)$$
$$- J_{q-2}(Tu)J_0(u)J_{q-2}(\Omega u)]$$
$$- \frac{\kappa_{01}\rho}{\beta_{01}\beta}\{J_{q+1}(Tu)J_1(u)[J_q(\Omega u) + J_{q+2}(\Omega u)]$$
$$+ J_{q-1}(Tu)J_1(u)[J_q(\Omega u) + J_{q-2}(\Omega u)]\},$$ (B3)

$$I_q^{p\leftarrow p}(u) = 2\left(\frac{n_{\mathrm{core}}k}{\beta} + 1\right)J_q(Tu)J_0(u)J_q(\Omega u)$$
$$- \left(\frac{n_{\mathrm{core}}k}{\beta} - 1\right)[J_{q+2}(Tu)J_0(u)J_{q+2}(\Omega u)$$
$$+ J_{q-2}(Tu)J_0(u)J_{q-2}(\Omega u)]$$
$$- \frac{\kappa_{01}\rho}{\beta_{01}\beta}\{J_{q+1}(Tu)J_1(u)[J_q(\Omega u) - J_{q+2}(\Omega u)]$$
$$- J_{q-1}(Tu)J_1(u)[J_q(\Omega u) - J_{q-2}(\Omega u)]\},$$ (B4)

$$I_q^{s\leftarrow p}(u) = \left(\frac{n_{\mathrm{core}}k}{\beta} - 1\right)[J_{q+2}(Tu)J_0(u)J_{q+2}(\Omega u)$$
$$- J_{q-2}(Tu)J_0(u)J_{q-2}(\Omega u)]$$
$$+ \frac{\kappa_{01}\rho}{\beta_{01}\beta}\{J_{q+1}(Tu)J_1(u)[J_q(\Omega u) - J_{q+2}(\Omega u)]$$
$$+ J_{q-1}(Tu)J_1(u)[J_q(\Omega u) - J_{q-2}(\Omega u)]\}.$$ (B5)

In these expressions Ω (in agreement with the definition in Section 3) and T are given by

$$\Omega = \frac{2K \tan \theta}{\kappa_{01}}, \qquad T = \frac{\tau}{\kappa_{01}}.$$ (B6)

ACKNOWLEDGMENTS

REFERENCES

1. G. Meltz, W. W. Morey, and W. H. Glenn, "Formation of Bragg gratings in optical fibers by a transverse holographic method," Opt. Lett. **14,** 823–825 (1989).
2. V. Mizrahi, T. Erdogan, D. J. DiGiovanni, P. J. Lemaire, W. M. MacDonald, S. G. Kosinski, S. Cabot, and J. E. Sipe, "Four channel fibre grating demultiplexer," Electron. Lett. **30,** 780–781 (1994).
3. G. Meltz, W. W. Morey, and W. H. Glenn, "In-fiber Bragg grating tap," presented at the Optical Fiber Communications Conference, San Francisco, Calif., January 22–26, 1990, paper TuG1.
4. R. Kashyap, R. Wyatt, and R. J. Campbell, "Wideband gain flattened erbium fibre amplifier using a photosensitive fibre blazed grating," Electron. Lett. **29,** 154–156 (1993).
5. V. Mizrahi and J. E. Sipe, "Optical properties of photo-sensitive fiber phase gratings," J. Lightwave Technol. **11,** 1513–1517 (1993).
6. K. O. Hill, B. Malo, K. A. Vineberg, F. Bilodeau, D. C. Johnson, and I. Skinner, "Efficient mode conversion in telecommunication fibre using externally written gratings," Electron. Lett. **26,** 1270–1272 (1990).
7. J. E. Sipe and G. I. Stegeman, "Comparison of normal mode and total field analysis techniques in planar integrated optics," J. Opt. Soc. Am. **69,** 1676–1683 (1979).
8. H. Kogelnik, "Theory of optical waveguides," in *Guided-Wave Optoelectronics,* T. Tamir, ed. (Springer-Verlag, Berlin, 1990).
9. D. Marcuse, *Theory of Dielectric Optical Waveguides* (Academic, Boston, 1991), Chap. 2.
10. J. E. Sipe, L. Poladian, and C. Martijn deSterke, "Propagation through nonuniform grating structures," J. Opt. Soc. Am. A **11,** 1307–1320 (1994).
11. D. Gloge, "Weakly guiding fibers," Appl. Opt. **10,** 2252–2258 (1971).
12. H. Kogelnik and C. V. Shank, "Coupled-wave theory of distributed feedback lasers," J. Appl. Phys. **43,** 2327–2335 (1972).
13. P. J. Lemaire, R. M. Atkins, V. Mizrahi, K. L. Walker, K. S. Kranz, and W. A. Reed, "High pressure H_2 loading as a technique for achieving ultrahigh UV photosensitivity and thermal sensitivity in GeO_2 doped optical fibres," Electron. Lett. **29,** 1191–1193 (1993).
14. A. S. Davydov, *Quantum Mechanics* (Pergamon, New York, 1965), Sect. 80.
15. L. I. Schiff, *Quantum Mechanics,* 3rd ed. (McGraw-Hill, New York, 1968), Sect. 35.